Monthly Notices
of the
ROYAL ASTRONOMICAL SOCIETY

Mon. Not. R. Astron. Soc. **425,** 907–929 (2012) doi:10.1111/j.1365-2966.2012.21272.x

A combined optical and X-ray study of unobscured type 1 active galactic nuclei – III. Broad-band SED properties

Chichuan Jin,⋆ Martin Ward and Chris Done

Department of Physics, University of Durham, South Road, Durham DH1 3LE

Accepted 2012 May 9. Received 2012 May 8; in original form 2012 February 24

ABSTRACT

In this third paper in a series of three, we present a detailed study of the broad-band spectral energy distribution (SED) of active galactic nuclei (AGNs) based on a nearby unobscured type 1 AGN sample. We perform a systematic cross-correlation study of several key parameters, i.e. $\Gamma_{2-10\,\mathrm{keV}}$, $L_{2-10\,\mathrm{keV}}$, $L_{\mathrm{bol}}/L_{\mathrm{Edd}} = \lambda_{\mathrm{Edd}}$, $L_{\mathrm{bol}}/L_{2-10\,\mathrm{keV}} = \kappa_{2-10\,\mathrm{keV}}$, $L_{\mathrm{bol}}/L_{5100\,\text{Å}} = \kappa_{5100\,\text{Å}}$, $\mathrm{FWHM}_{\mathrm{H}\beta}$, M_{BH}, α_{ox}, α_{X} and α_{UV}. The well-defined spectral properties of the sample enable us to improve existing relations and to identify new correlations among these parameters. We confirm a break region around $\mathrm{FWHM}_{\mathrm{H}\beta} \simeq 4000\,\mathrm{km\,s^{-1}}$ in the $\Gamma_{2-10\,\mathrm{keV}}$ versus $\mathrm{FWHM}_{\mathrm{H}\beta}$ correlation and $\log(M_{\mathrm{BH}}) \simeq 8.0$ in the $\Gamma_{2-10\,\mathrm{keV}}$ versus M_{BH} correlation, where these correlations appear to change form. Beyond the break point, the intrinsic $\Gamma_{2-10\,\mathrm{keV}}$ index is dispersed around 1.8. Several new correlations are also reported in this paper, e.g. strong correlations in κ_{5100} versus λ_{Edd}, κ_{5100} versus $\kappa_{2-10\,\mathrm{keV}}$ and $\kappa_{2-10\,\mathrm{keV}}$ versus M_{BH}. The principal component analysis (PCA) is performed on the correlation matrix of the above parameters. This shows that the three physical parameters, i.e. black hole mass, mass accretion rate and Eddington ratio, drive the majority of the correlations. This is consistent with PCA results found from previous optical spectral studies.

For each key parameter, we split the AGNs into three subsamples, binned based on increasing value of that parameter. We co-add the model SEDs for each object in the subsample to see how the SED changes with that parameter. Most parameters, except L_{bol}, show similar systematic changes in the SED such that the temperature at which the disc peaks is correlated with the ratio of power in the disc versus the Comptonized components and the hard X-ray spectral index. This underlying change in SED shape shows that AGNs do exhibit intrinsically different spectral states. This is superficially similar to the SED differences in black hole binary (BHB) seen as λ_{Edd} increases, but the analogy does not hold in detail. Only objects with the highest λ_{Edd} appear to correspond to a BHB spectral state (the disc-dominated high/soft state). The AGNs with typical mass accretion rates have spectra which do not match well with any state observed in BHB. We speculate that this could be due to the presence of a powerful ultraviolet line-driven disc wind, which complicates simple mass scaling between stellar and supermassive black holes.

Key words: accretion, accretion discs – galaxies: active.

1 INTRODUCTION

The broad-band spectral energy distribution (SED) of active galactic nuclei (AGNs) has been studied for many years. The unobservable gap between the extreme-ultraviolet (EUV) and soft X-rays, imposed by Galactic photoelectric absorption, sets a major barrier to reconstructing the overall SED. This is particularly problematic because it is in this energy range that the peak of the SED often occurs. Due to this difficulty, most previous work focused on spectral properties of either the optical/UV side (e.g. Sanders et al. 1989; Francis et al. 1991; Zheng et al. 1997; Vanden Berk et al. 2001) or the X-ray side (e.g. Wilkes & Elvis 1987; Green et al. 1995; George et al. 2000). However, the multiwavelength combination is required to see the overall SED behaviour (e.g. Elvis et al. 1994; Laor et al. 1997; Shang et al. 2005; Richards et al. 2006; Lusso et al. 2010, hereafter Lusso10). In order to recover the spectral shape in the UV/soft X-ray gap, some studies simply connected the optical/UV

⋆E-mail: chichuan.jin@durham.ac.uk

and X-ray spectra to estimate the SED (e.g. Elvis et al. 1994; Shang et al. 2005; Richards et al. 2006; Lusso10). As the origin of the optical and hard X-ray emission became clearer, more broad-band SED models with multiple physical components were used to fit the multiwaveband spectra. These were used to extrapolate across the UV gap based on the model assumptions, but with better justification than before (e.g. Middleton, Done & Gierliński 2007; Vasudevan & Fabian 2007, hereafter VF07; Vasudevan & Fabian 2009, hereafter VF09; Jin et al. 2009; Grupe et al. 2010, hereafter Grupe10). For example, VF07 used a power law plus accretion disc model to construct the broad-band SED for their sample. This technique was repeated in VF09 based on 29 AGNs from the reverberation mapping sample (Peterson et al. 2004), and using simultaneous optical/UV and X-ray data from *XMM–Newton*. Grupe10 used an absorbed power law for the X-ray spectrum, and an exponentially cut-off power law (or a broken power law) for the optical/UV spectrum, to construct the broad-band SED for their sample, for which simultaneous optical, UV and X-ray data are available from *Swift*. Further discussion of some previous SED studies is given in Jin et al. (2012, hereafter Paper I).

Within these works, some specific AGN parameters were studied, including black hole mass ($M_{\rm BH}$), Eddington ratio ($L/L_{\rm Edd} = \lambda_{\rm Edd}$), bolometric luminosity ($L_{\rm bol}$), 2–10 keV luminosity ($L_{2-10\,\rm keV}$), 2–10 keV photon index ($\Gamma_{2-10\,\rm keV}$) and Hβ full width at half-maximum (FWHM). Also, some parameters directly related to the broad-band SED shape were proposed, such as the optical to X-ray spectral index ($\alpha_{\rm ox}$;[1] Tananbaum et al. 1979), 2–10 keV bolometric correction ($\kappa_{2-10\,\rm keV}$, defined as $L_{\rm bol}/L_{2-10\,\rm keV}$; e.g. VF07), 5100-Å luminosity scaling factor (κ_{5100}, defined as $L_{\rm bol}/L_{5100}$, where L_{5100} is the monochromatic luminosity at 5100 Å; Kaspi et al. 2000).

Since the number of AGNs with both high-quality optical/UV and X-ray spectra is relatively small, much effort is devoted to search for correlations among the key SED parameters, especially those parameters capable of representing the broad-band SED shape. Then, for those many AGNs lacking sufficient spectral information, these correlations can be used to predict the SEDs that cannot be defined from direct observation. Indeed, many such parameter correlations have been proposed. For example, VF07 reported a strong correlation between $\kappa_{2-10\,\rm keV}$ and $\lambda_{\rm Edd}$ (VF07; VF09; Lusso10). Correlations were also found between Hβ FWHM and $\Gamma_{2-10\,\rm keV}$ (e.g. Leighly 1999; Reeves & Turner 2000; Shemmer et al. 2006, hereafter S06; Shemmer et al. 2008, hereafter S08; Zhou & Zhang 2010a, hereafter Zhou10a), $\lambda_{\rm Edd}$ and $\Gamma_{2-10\,\rm keV}$ (e.g. Lu & Yu 1999; Porquet et al. 2004; Wang, Watarai & Mineshige 2004; Bian 2005; S06; S08) and Hβ FWHM and $\lambda_{\rm Edd}$ (e.g. Grupe10; Paper I). The correlation between L_{2500} and $L_{2\,\rm keV}$ is another important result, which led to further correlation studies related to $\alpha_{\rm ox}$, L_{2500}, $L_{2\,\rm keV}$ and redshift (e.g. Green et al. 2009, see references given in Table 2). In Table A1 (see Supporting Information with the online version of the paper), we list some of the principal parameters and the relevant papers discussing the correlations. Later in the paper, we will discuss some additional correlations, e.g. $M_{\rm BH}$ versus $\Gamma_{2-10\,\rm keV}$ and $M_{\rm BH}$ versus $\kappa_{2-10\,\rm keV}$, in the context that changes in these parameters are caused by changes in the fundamental physical processes.

However, due to the difficulty in obtaining and analysing both optical/UV and X-ray spectra for a large sample, these parameter correlations are reported separately and based on different samples, rather than being studied systematically for a single well-defined sample. Furthermore, most of the previous samples were not selected based on their spectral properties, so effects such as reddening will introduce biases into the cross-correlations. The lack of a self-consistent physically motivated broad-band model has also been a constraint to performing a more detailed SED study.

In Paper I, we defined a sample of 51 type 1 AGNs with both optical/UV and X-ray spectra which are of high quality, and without evidence of complex spectral absorption features, e.g. a warm absorber. Based on this bright and unobscured type 1 AGN sample, we applied our latest optical and broad-band SED model to perform the spectral fitting, and so matched the optical spectrum and produced a broad-band SED for each AGN in the sample. This is so far the most detailed spectral analysis for a medium sized sample of AGNs, with such well-defined high-quality spectra. In our preceding paper (Jin, Ward & Done 2012b, hereafter Paper II), we studied the Balmer emission-line properties and the relation between the optical and X-ray emission, based on the same sample and the spectral fitting results given in Paper I. This paper is based on the sample of Paper I, but focuses on the shape of the broad-band SED, and how this relates to a range of parameters from the model. We will approach this problem by first investigating the numerous correlations previously reported. Then a set of mean SEDs based on key parameters are constructed and studied in detail.

These mean SEDs show a clear change in shape as a function of the AGN parameters, probably most fundamentally driven by a change in $\lambda_{\rm Edd}$. The SED becomes more disc dominated and the X-ray tail softens as $\lambda_{\rm Edd}$ increases (e.g. Grupe10). This is superficially similar to the changes seen in the Galactic black hole binary (BHB) systems as the mass accretion rate increases. In BHB at low Eddington ratio ($\lambda_{\rm Edd} \leq 0.02$) the X-ray spectra are hard, $\Gamma_{2-10\,\rm keV} < 2$, and the disc emission is weak (low/hard state). As the mass accretion rate increases, the disc increases in importance relative to the tail, and the tail steepens until it reaches the disc-dominated 'thermal state' (also known as the high/soft state) where the power-law tail is somewhat steeper $\Gamma_{2-10\,\rm keV} \sim 2$–2.2. At high Eddington fractions, the source can also show a 'very high' or steep power-law state, where both disc and tail contribute to the spectra, but the spectra are typically steep ($\Gamma_{2-10\,\rm keV} \geq 2.2$) (Remillard & McClintock 2006; Meyer-Hofmeister, Liu & Meyer 2009). It has been proposed that AGNs are simply scaled-up counterparts to the BHBs, so they should also show similar spectral states (Done & Gierliński 2005; McHardy et al. 2006; Gierliński et al. 2008; Jin et al. 2009; Middleton et al. 2009). Therefore, the Eddington ratio may also be a good indicator of an AGN's accretion state, and so determine the shape of its SED, explaining the multiple strong correlations between various SED parameters.

This paper is organized as follows. Section 2 gives a brief description of the main characteristics of the sample and the method used for fitting the broad-band SED. Further details of this are presented in Paper I. In Section 3 we examine the parameter correlations across five parameter groups. Some significant new correlations are proposed. In Section 4 we perform a systematic study of all correlations among several selected key parameters and build a cross-correlation matrix. The principal component analysis (PCA) technique is used on this correlation matrix in order to derive the eigenvectors. In Section 5 various mean SEDs are constructed based on the mean values of the key parameters. In Section 6 we investigate further the reliability of these correlations, including the effect of a correction to the black hole mass from radiation pressure (RP). In Section 7 we summarize our results and propose topics for further study. A flat universe model with a Hubble constant of $H_0 = 72\,\rm km\,s^{-1}\,Mpc^{-1}$, $\Omega_{\rm M} = 0.27$ and $\Omega_\Lambda = 0.73$ is adopted throughout the paper.

[1] $\alpha_{\rm ox} = -\frac{\log(F(2\,\rm keV)/F(2500\,Å))}{2.605}$, assuming $F(\nu) \propto \nu^{-\alpha}$ to ensure a non-negative $\alpha_{\rm ox}$.

2 PROPERTIES OF THE SAMPLE AND BROAD-BAND SED MODELLING

2.1 Sample selection and properties

The AGN sample used in this paper is reported in Paper I, based on the cross-correlation between the Sloan Digital Sky Survey (SDSS) Data Release 7 (DR7) and *XMM–Newton* catalogues. The complete source list, detailed sample selection criteria and sample properties can be found in Paper I. The main selection steps are summarized below.

(1) We searched the 2XMMi and SDSS DR7 catalogues and identified 3342 extragalactic sources having both X-ray and optical spectra.

(2) Within these sources, we selected those with Hβ in emission and redshift $z < 0.4$, so that both the Hα and Hβ emission lines are covered by the SDSS spectra. This assists with modelling of the Balmer lines (see Paper I). This selection resulted in 802 unique X-ray sources.

(3) Within this subsample, we identified 96 type 1 AGNs all with a minimum of 2000 counts in at least one of the three *XMM–Newton* EPIC cameras to ensure high X-ray spectral quality.

(4) We then excluded 23 sources whose Hβ line was modified due to high reddening, low signal-to-noise ratio (S/N) or a data gap in the SDSS spectra. The resulting sample contains 73 AGNs.

(5) For each of the 73 sources, a power-law model was fitted to the rest-frame 2–10 keV X-ray spectra. The 16 objects with photon index uncertainties greater than 0.5 were excluded, leaving 57 type 1 AGNs with relatively well constrained 2–10 keV spectra.

(6) A further six objects were excluded because of an obvious signature of a warm absorber at ∼0.7 keV. This criterion means that the observed spectra are very likely directly related to emission from the bare central core.

The final sample contains 51 AGNs, with 12 AGNs classified as narrow-line Seyfert 1 galaxies (NLS1s) using the conventional definition (Goodrich 1989), while the others are all broad-line Seyfert 1 galaxies (BLS1s). The broad absorption line (BAL) quasar PG 1004+130 is also included in our sample whose weak and featureless X-ray emission is still under debate (Miller et al. 2006). The vast majority of the sample are radio-quiet (RQ) with only three radio-loud (RL) sources, i.e. PG 1004+130, RBS 0875 and PG 1512+370.

The Hβ FWHM of the sample ranges from 600 to 13 000 km s^{-1}.

2.2 The spectral modelling

Based on the high-quality spectra, Paper I conducted detailed spectral analysis for each source in the sample. In the optical spectral fitting, the Hα and Hβ lines were fitted using three components. The narrow component has the same profile as the entire [O III] λ5007 line, i.e. including both the central and blue components in [O III] λ5007. The intermediate and broad components are assumed to have the shape of a Gaussian. All other strong nearby emission lines are included by adding more Gaussian profiles into the whole model. Then a complete model with multiple components were used to fit the whole SDSS spectra, including the underlying continuum approximated by a power law, the Balmer continuum, the Fe II 'false' continuum and all strong emission lines. The broad-band SED model used in Paper I (optxagn, hereafter Model A) consists of the following three continuum components: (1) emission from a modified standard accretion disc, whose energy within the corona radius is completely reprocessed into the other two high-energy Comptonization components; (2) emission from the low-temperature, optically thick Comptonization, which mainly accounts for the soft X-ray excess; and (3) emission from the high-temperature, optically thin Comptonization which gives the power-law shape of the hard X-ray spectrum above 2 keV. Both Galactic extinction and the small amount of intrinsic reddening/extinction are included in the model.

Because the model was in the process of development, Paper I did not consider the effect of a colour temperature correction in the accretion disc model (e.g. Ross, Fabian & Mineshige 1992; Davis & Hubeny 2006). This effect is due to the fact that the absorption opacity decreases significantly as the black hole mass increases ($\kappa_{\rm abs} \propto M^{-1/8}$; Done et al. 2012), so for the same Eddington ratio, AGN's disc has a lower absorption opacity than BHB. Then for some AGNs, the accretion disc may no longer be locally thermalized. The higher temperature photons can emerge from deeper regions in the disc, and so the disc spectrum extends to higher energy than for standard accretion disc spectrum, producing the effect of a colour temperature correction. However, this can only happen for disc regions of $T > 3 \times 10^4$ K where sufficient hydrogen atoms are ionized. In addition, the electron scattering opacity also becomes important in these regions. The lower energy electrons in the surface regions Compton down-scatter the higher temperature photons from deeper disc regions, thus reducing the colour temperature correction. These two competing effects lead to an effective colour temperature correction (Davis, Done & Blaes 2006).

The maximum effective temperature of the accretion disc is $kT \sim 10(\dot{m}/M_8)^{1/4}$ eV (where $\dot{m} = L_{\rm bol}/L_{\rm Edd}$, $M_8 = M/10^8\,{\rm M}_\odot$), so only for AGNs with low-mass black holes and high-mass accretion rates such as the NLS1s (e.g. Boller, Brandt & Fink 1996; Paper I) will electron scattering opacity dominate, and the effect of colour temperature correction becomes important. A typical colour temperature correction of 2.6 is predicted for an AGN with $M_{\rm BH} = 10^6\,{\rm M}_\odot$ and $\lambda_{\rm Edd} = 1.0$ (Davis et al. 2006; Done et al. 2012). This effect combines with an already hot disc due to the low black hole mass, resulting in a disc spectrum that extends significantly into the soft X-ray range.

A more detailed explanation of this colour temperature correction in AGN can be found in Done et al. (2012), where a model (optxagnf in XSPEC v12) is proposed which applies a colour temperature correction for the Comptonized accretion disc model (hereafter Model B). In this paper we use this more advanced model to fit the optical, UV and X-ray data so as to construct the broad-band SED for each source. Fig. 1 shows an example of the broad-band SED fitting to the multiwaveband spectra of RBS 769. A detailed description of Model B in comparison with Model A can be found in Done et al. (2012). The set of fitting parameters for each source, based on Model B, is given in Table B1 (see Supporting Information with the online version of the paper). Section 6.3 discusses the statistical differences resulting from using Model B and Model A for our sample.

All the principal SED parameters such as $\lambda_{\rm Edd}$, $\kappa_{2-10\,{\rm keV}}$ and $\alpha_{\rm ox}$ are calculated from the new model fitting (see Table B2 with the Supporting Information). A cross-correlation study of the various parameters is then conducted. In Table 1 we compare the mean values of some SED parameters of our sample with those samples used in previous work. The result of correlations established in these previous studies will be compared with ours in the following sections.

There are two sources that we treated as being anomalous in our study. The first is PG 1004+130, a BAL quasar, whose X-ray

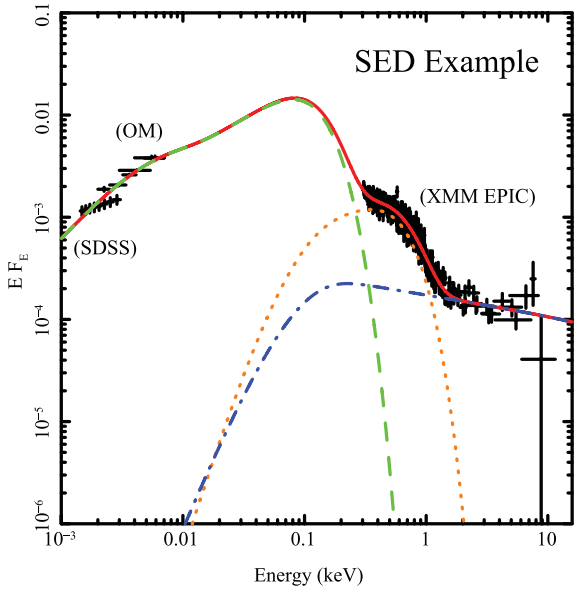

Figure 1. An example of the broad-band SED fitting using optxagnf model in XSPEC v12 which includes the effect of a colour correction. The data are taken from SDSS and *XMM–Newton* observations of RBS 769. The solid red line shows the total model; the dashed green line shows the colour corrected and truncated accretion disc emission; the dotted orange line shows the low-temperature optically thick Comptonization; the dot–dashed blue line shows the high-temperature optically thin Comptonization. The reduced χ^2 is 1.16 for this spectral fitting.

was reported as being extraordinarily weak. Although its X-ray spectrum does not show clear absorption edges, it is nevertheless likely to be heavily absorbed, so that the remaining X-rays may have a different origin such as a sub-parsec-scale jet. It has been suggested that the X-ray emission from PG 1004+130, after correcting for its intrinsic absorption, is 0.73 dex weaker than normal PG RL quasars normalized to similar optical/UV luminosities (Miller et al. 2006). Due to its distinct X-ray spectrum (and correspondingly different X-ray parameters), we did not include this source in our regression analysis. The other anomalous source is Mrk 110. This source shows strong optical variability (Kollatschny et al. 2001; Kollatschny 2003), and its SDSS spectrum has a different slope from the (non-simultaneous) *XMM–Newton* OM data (see Paper I). However, the optical spectrum obtained using FAST shown in Landt et al. (2011) is consistent with the OM data, and is also an order of magnitude brighter than the SDSS spectrum. Therefore, the SDSS spectrum of Mrk 110 is not consistent with its broad-band SED parameters, and so we exclude Mrk 110 from any correlation which depends on optical parameters, but include it for any UV/X-ray correlations.

3 INVESTIGATING THE CORRELATIONS FOR VARIOUS SED PARAMETER GROUPS

In this section we divide the SED parameters into several subgroups, based on correlations reported in the literature (see Section 1), and then perform a cross-correlation analysis within each group.

3.1 Group 1: L_{2500}, $L_{2\,\mathrm{keV}}$ and α_{ox}

The α_{ox} index has been used as the indicator of the SED shape for more than 30 years. It is often used as an indication of the AGN's broad-band SED and to convert between the AGN's optical luminosity function and X-ray luminosity function (e.g. Hopkins, Richards & Hernquist 2007, hereafter Hopkins07; Tang, Zhang & Hopkins 2007, hereafter Tang07).

Many studies have been carried out on the evolution of α_{ox} with luminosity (e.g. Avni & Tananbaum 1982; Wilkes et al. 1994; Strateva et al. 2005; Steffen et al. 2006; Just et al. 2007; Green et al. 2009, hereafter Green09; Grupe10; Lusso10), which may provide clues on the emission mechanism. The value of α_{ox} has been found to be in the range 1.2–1.8, with a mean value of ∼1.5. Correlations have also been found between $L_{2\,\mathrm{keV}}$, L_{2500} and α_{ox}, with the primary correlation being $L_{2\,\mathrm{keV}} \propto L_{2500}^{\beta}$. The slope index β was often found to deviate from unity for both optically selected (e.g. Strateva et al. 2005; Steffen et al. 2006; Just et al. 2007) and X-ray selected AGN samples (e.g. Lusso10). However, La Franca et al. (1995) re-analysed the Wilkes et al. (1994) sample by considering both variables and intrinsic scattering, and found that β was consistent with unity. Green09 collected a large, well-defined sample of 2308 SDSS/ChaMP quasi-stellar objects (QSOs) in the redshift range 0.2–5.4, and concluded that β is not less than unity.

The reality of a non-linear correlation in $L_{2\,\mathrm{keV}}$ versus L_{2500} remains an open question, but one possible explanation could be a selection effect in a flux-limited sample for which dispersions in the optical and X-ray luminosity are not equal or which change with cosmic time (Yuan, Siebert & Brinkmann 1998, hereafter Yuan98; Tang07). However, the possibility of a truly intrinsic non-linear correlation cannot be ruled out. A non-linear $L_{2\,\mathrm{keV}}$ versus L_{2500} correlation implies that there is a dependence of α_{ox} on $L_{2\,\mathrm{keV}}$ and L_{2500}

Table 1. The mean parameter values with one standard deviation for our sample, together with some recently published samples. N: sample size. κ_{2-10}: the 2–10 keV bolometric correction. Lusso10: Lusso et al. (2010); Grupe10: Grupe et al. (2010); Zhou10a: Zhou & Zhang (2010a); VF07 and VF09: Vasudevan & Fabian (2007) and Vasudevan & Fabian (2009), respectively.

Sample	N	Redshift	$\Gamma_{2-10\,\mathrm{keV}}$	κ_{2-10}	κ_{5100}	λ_{Edd}	$\mathrm{FWHM}_{\mathrm{H}\beta}$ ($\mathrm{km\,s^{-1}}$)	M_{BH} $\log(\mathrm{M}_{\odot})$	α_{ox}	L_{bol} $\log(\mathrm{erg\,s^{-1}})$
This work	51	$0.137^{+0.158}_{-0.073}$	1.91 ± 0.26	38^{+58}_{-23}	15^{+14}_{-7}	$0.27^{+0.61}_{-0.19}$	3560^{+3880}_{-1860}	7.93 ± 0.52	1.35 ± 0.14	45.47 ± 0.57
Lusso10	545	$1.440^{+1.020}_{-0.597}$	–	27^{+28}_{-14}	–	–	–	–	1.40 ± 0.16	45.54 ± 0.57
Grupe10	92	0.112 ± 0.077	–	–	21 ± 3	1.87 ± 3.26	2670 ± 1670	7.37 ± 0.73	1.42 ± 0.17	45.00 ± 0.96
Zhou10a	[a]69	$0.050^{+0.103}_{-0.034}$	1.97 ± 0.29	–	–	[b]$0.24^{+0.76}_{-0.18}$	2600^{+2500}_{-1280}	–	–	–
VF09	29	$0.033^{+0.074}_{-0.023}$	1.85 ± 0.32	28^{+74}_{-20}	–	0.18 ± 0.16	–	[c]7.93 ± 0.66	1.39 ± 0.24	44.89 ± 1.00
VF07	54	$0.064^{+0.147}_{-0.044}$	–	26^{+39}_{-16}	–	$0.15^{+0.76}_{-0.13}$	–	7.89 ± 0.82	–	45.20 ± 1.01

[a]There are 114 sources in Zhou10a, but we only consider the 69 NLS1s and BLS1s with both Hβ FWHM and λ_{Edd} measurements.
[b]The Eddington ratios were calculated using the luminosity-dependent 2–10 keV bolometric correction in Marconi04.
[c]The black hole masses are from the reverberation mapping study in Peterson et al. (2004).

(e.g. Vignali, Brandt & Schneider 2003; Just et al. 2007; Lusso10), but this is still a matter of debate (Yuan98; Tang07).

To further test the basis of these correlations, we also calculated the values of $L_{2\,\mathrm{keV}}$, L_{2500} and α_{ox} from our best-fitting model of the SEDs, and then performed the same cross-correlation analysis. The limitation of our results arises from the lack of actual spectral coverage at 2500 Å for the 16 sources without OM *UVW1* and *UVM2* data. The luminosity and redshift range of our sample is also relatively small. However, on the merit side we have included two inputs of reddening/absorption to model both the Galactic and the AGN's intrinsic extinction during the broad-band SED fitting, so our values of $L_{2\,\mathrm{keV}}$, L_{2500} and α_{ox} should be closer to those of the intrinsic source. The unobscured nature of our sample and the exclusion of warm absorber sources also help reduce uncertainties in the corrections caused by reddening/absorption.

3.1.1 *The $L_{2\,\mathrm{keV}}$ versus L_{2500} correlation*

Fig. 2 shows our $L_{2\,\mathrm{keV}}$ versus L_{2500} correlation. The statistical methods used are the same as in Lusso10, i.e. we use the full parametric estimate and expectation-maximization (EM) algorithm. We use this to derive two regression lines assuming first $L_{2\,\mathrm{keV}}$, then L_{2500} to be the independent variable. Then the bisector of the two regression lines is calculated using the equations in Isobe et al. (1990). This method is more appropriate in cases where the cross-correlations are dominated by intrinsic scatter. The correlations found are as follows:

(i) the EM regression line when L_{2500} is assumed to be the independent variable is

$$\log(L_{2\,\mathrm{keV}}) = (0.83 \pm 0.05)\log(L_{2500}) + (1.59 \pm 1.55); \quad (1)$$

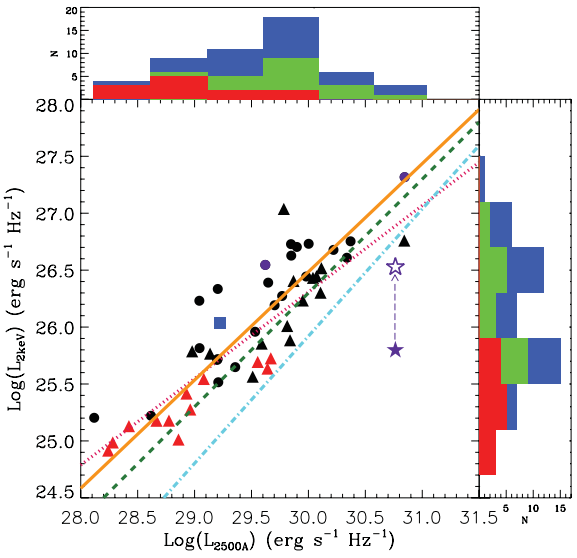

Figure 2. The cross-correlation between L_{2500} and $L_{2\,\mathrm{keV}}$. The solid orange line is the bisector regression line for our sample. The red triangle symbols represent NLS1s; purple symbols show the RL AGN; the blue square symbol is Mrk 110. The filled purple star is the BAL quasar PG 1004+130, and the open purple star is the position if its intrinsic X-ray flux was 0.73 dex higher (Miller et al. 2006). All triangle symbols represent population A sources whose Hβ FWHM is less than 4000 km s^{-1}. In the two histograms, the green and red regions are for the population A sources, and the red region indicates the 12 NLS1s. The dashed green line is based on Hasinger05; the dot–dashed cyan line is based on Green09; the dotted pink line is based on Lusso10.

(ii) the EM regression line when $L_{2\,\mathrm{keV}}$ is assumed to be the independent variable is

$$\log(L_{2\,\mathrm{keV}}) = (1.09 \pm 0.09)\log(L_{2500}) - (6.17 \pm 2.66); \quad (2)$$

(iii) the bisector of the above two regression lines (the solid orange line in Fig. 2) is

$$\log(L_{2\,\mathrm{keV}}) = (0.95 \pm 0.06)\log(L_{2500}) - (2.04 \pm 1.77). \quad (3)$$

The Spearman's rank test gives a rank coefficient of $\rho_{\mathrm{s}} = 0.87$, and the probability of deviation from a random distribution is $d_{\mathrm{s}} = 1.2 \times 10^{-16}$, confirming a very high level of significance. We superimpose PG 1004+130 (filled purple star) on Fig. 2, showing that it lies far from the correlation due to its unusual X-ray weakness. It matches much better to the regression line if corrected in $L_{2\,\mathrm{keV}}$ by 0.73 dex (the empty purple star in Fig. 2; Miller et al. 2006).

Our correlation between $L_{2\,\mathrm{keV}}$ and L_{2500} is close to linear, but previous studies have found a wide range of values as listed in Table 2. Fig. 2 plots these results for comparison. The correlation found by Hasinger (2005, hereafter Hasinger05) (green dashed line), which is based on an X-ray selected sample, is the most consistent with our sample, whereas the slope found by Lusso10 (pink dashed line) is significantly flatter. Our slope is also consistent with Green09 (cyan dashed line) in which a large sample of optically selected quasars is analysed. We note that our sample only covers the low-luminosity region of the sample in Green09. The NLS1s are the least luminous sources. The different value of the Y-axis intercept in Green09 may be due to their larger sample and larger luminosity dispersion.

There can be several reasons for the difference between our results and Lusso10. First, there may be a selection effect of a flux-limited sample if there are different amounts of dispersion in optical and X-ray luminosities (Yuan98; Tang07). More importantly, our sample is corrected for both Galactic and intrinsic reddening/absorption in the host Galaxy through the spectral fitting, whereas that of Lusso10 is only corrected for Galactic absorption. We remove the intrinsic reddening correction and recompute the EM regression, with results given in Table 2 under the row 'This work-r_{int}'. The dust reddening and gas absorption column are related by $E(B-V) = 1.7 \times (N_{\mathrm{H}}/10^{22})\,\mathrm{cm}^{-2}$ (Bessell 1991), which means that L_{2500} is suppressed much more severely than $L_{2\,\mathrm{keV}}$. Hence the removal of intrinsic reddening correction decreases our correlation slope from 0.95 (±0.06) to 0.91 (±0.05). Thus the intrinsic reddening can flatten the correlation, but it does not seem to be enough on its own to explain the difference with Lusso10, unless their sample is strongly reddened in the optical.

3.1.2 *The α_{ox} versus $L_{2\,\mathrm{keV}}$ and α_{ox} versus L_{2500} correlations*

To further investigate the correlation between the optical/UV and X-ray continua, we adopt the same approach as in previous work to produce α_{ox} versus L_{2500} and α_{ox} versus $L_{2\,\mathrm{keV}}$ correlations. If we assume $L_{2\,\mathrm{keV}} \propto L_{2500}^{\beta}$, then $\alpha_{\mathrm{ox}} \propto L_{2500}^{1-\beta}$ and $\alpha_{\mathrm{ox}} \propto L_{2\,\mathrm{keV}}^{\beta(1-\beta)}$ are expected by definition. However, the Spearman's rank test does not imply very strong correlations: $\rho_{\mathrm{s}} = 0.31$ and $d_{\mathrm{s}} = 0.03$ for α_{ox} versus L_{2500}; $\rho_{\mathrm{s}} = -0.13$ and $d_{\mathrm{s}} = 0.35$ for α_{ox} versus $L_{2\,\mathrm{keV}}$. The regression lines were derived but with a large uncertainty. The results are presented in Fig. 3 and listed in Table 2. The solid orange line in each panel of Fig. 3 is our EM regression line, compared with some previous work shown by dashed lines. Note that our results are limited to redshift $z < 0.4$, $L_{2500} < 10^{+31}$ erg s^{-1} Hz^{-1} and

Table 2. Comparison of regression line coefficients for $L_{2\,\mathrm{keV}}$, L_{2500}, α_{ox} and redshift correlations. Lusso10: Lusso et al. (2010); Grupe10: Grupe et al. (2010); Green09: Green et al. (2009); Just07: Just et al. (2007); Steffen06: Steffen et al. (2006); Strateva05: Strateva et al. (2005); Hasinger05: Hasinger (2005). opt: optically selected sample. xray: X-ray selected sample.

Sample	$L_{2\,\mathrm{keV}}$ versus L_{2500}		α_{ox} versus L_{2500}		α_{ox} versus $L_{2\,\mathrm{keV}}$	
	β_1^{bi}	ξ_1^{bi}	β_2^{em}	ξ_2^{em}	β_3^{em}	ξ_3^{em}
[a]This work	0.95 ± 0.06	-2.04 ± 1.77	0.07 ± 0.02	-0.61 ± 0.60	-0.03 ± 0.03	2.17 ± 0.76
[b]This work-r_{int}	0.91 ± 0.05	-0.69 ± 1.68	0.08 ± 0.02	-0.92 ± 0.57	-0.01 ± 0.03	1.55 ± 0.76
Lusso10$^{\mathrm{xray}}$	0.76 ± 0.02	3.51 ± 0.64	0.15 ± 0.01	-3.18 ± 0.22	0.02 ± 0.01	0.86 ± 0.34
Grupe10$^{\mathrm{opt}}$	–	–	0.11 ± 0.01	-1.18 ± 0.31	–	–
Green09$^{\mathrm{opt}}$	1.12 ± 0.02	-7.59 ± 0.64	0.06 ± 0.01	-0.32 ± 0.26	0.10 ± 0.01	1.38 ± 0.21
Just07$^{\mathrm{opt}}$	0.71 ± 0.01	4.88 ± 0.63	0.14 ± 0.01	-2.71 ± 0.21	0.09 ± 0.01	-0.90 ± 0.36
Steffen06$^{\mathrm{opt}}$	0.72 ± 0.01	4.53 ± 0.69	0.14 ± 0.01	-2.64 ± 0.24	0.08 ± 0.02	-4.1 ± 0.39
Strateva05$^{\mathrm{opt}}$	0.65 ± 0.02[c]	6.73 ± 0.64[c]	0.14 ± 0.01[c]	-2.62 ± 0.25[c]	–	–
Hasinger05$^{\mathrm{xray}}$	1.0[d]	-3.7[d]	–	–	–	–

[a]Linear regression results using $L_{2\,\mathrm{keV}}$ and L_{2500} from the reconstructed broad-band SED corrected for both intrinsic and Galactic reddening/extinction.
[b]Linear regression when $L_{2\,\mathrm{keV}}$ and L_{2500} were not corrected for the best-fitting intrinsic reddening/extinction, but corrected for the Galactic value.
[c]For the SDSS main sample + high-z sample + Sy 1 sample (see Strateva05).
[d]Measured directly from the regression line in fig. 5(b) of Hasinger05.

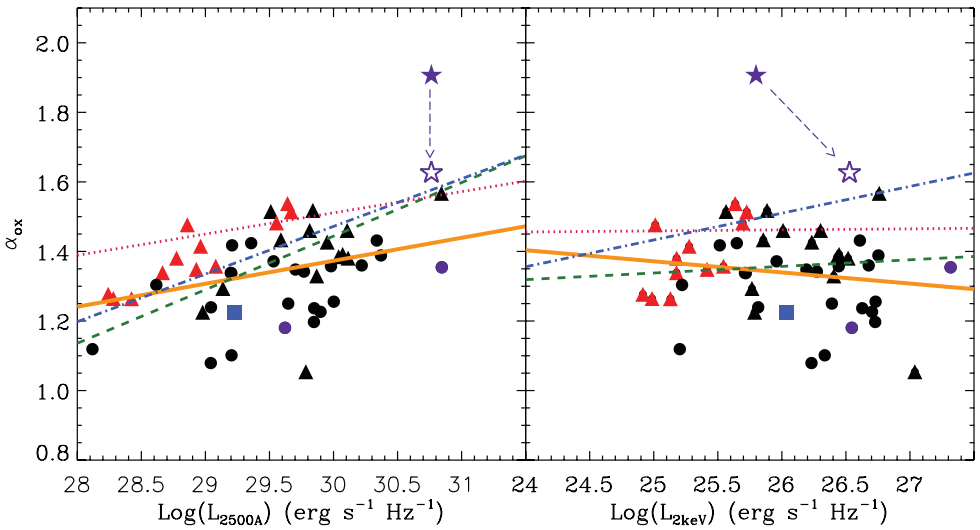

Figure 3. α_{ox} versus L_{2500} and α_{ox} versus $L_{2\,\mathrm{keV}}$. Each symbol represents the same type of source as in Fig. 2. In each panel, the solid orange line is the OLS regression line for our sample, assuming the X-axis variable to be the independent variable. The dot–dashed blue line is based on Steffen06, the dotted pink line on Green09 and the dashed green line on Lusso10.

$L_{2\,\mathrm{keV}} < 10^{+27.5}$ erg s^{-1} Hz^{-1}. Our results also suggest that the cross-correlations in α_{ox} versus L_{2500} and α_{ox} versus $L_{2\,\mathrm{keV}}$ are dominated by the AGN's intrinsic dispersion.

3.2 Group 2: α_{ox}, $\kappa_{2-10\,\mathrm{keV}}$ and λ_{Edd}

As mentioned in the previous section, α_{ox} is often used as a proxy for the broad-band SED shape. L_{bol} is often dominated by the big blue bump (BBB) peaking in the unobservable EUV region (Walter & Fink 1993). $\kappa_{2-10\,\mathrm{keV}}$, defined as $L_{\mathrm{bol}}/L_{2-10\,\mathrm{keV}}$, is also an indicator of the SED shape. λ_{Edd} is an important parameter which relates directly to the accretion processes close to the central supermassive black hole (SMBH). Therefore, correlations are to be expected between λ_{Edd}, $\kappa_{2-10\,\mathrm{keV}}$ and α_{ox}.

3.2.1 *The α_{ox} versus $\kappa_{2-10\,keV}$ correlation*

Lusso10 reported a tight second-order polynomial correlation for $\kappa_{2-10\,\mathrm{keV}}$ versus α_{ox}. We find a similar correlation for our sample. Spearman's rank test shows $\rho_{\mathrm{s}} = 0.73$ and $d_{\mathrm{s}} = 2 \times 10^{-9}$. We also fitted a second-order polynomial to the correlation and obtained the following equation:

$$\log(\kappa_{2-10}) = (5.7 \pm 3.4) - (8.8 \pm 5.2)\alpha_{\mathrm{ox}} + (4.3 \pm 2.0)\alpha_{\mathrm{ox}}^2. \quad (4)$$

Fig. 4 shows our best-fitting polynomial (solid orange line) with $\pm 1\sigma$ dispersion region (the shaded region). Note that our fit excludes BAL quasar PG 1004+130 (purple star in Fig. 4). The best-fitting polynomial from Lusso10 is plotted as the dashed green line, which is not as steep as ours. The reason is that our value of $\kappa_{2-10\,\mathrm{keV}}$ (and L_{bol}) is higher than found by Lusso10,

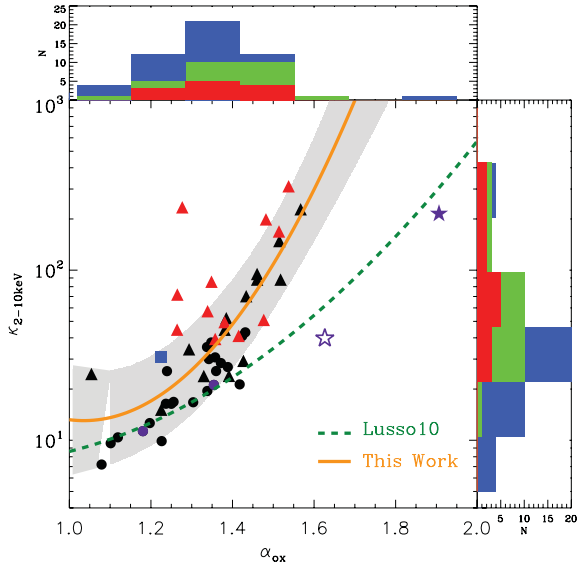

Figure 4. $\kappa_{2-10\,\mathrm{keV}}$ versus α_{ox}. Each symbol represents the same type of source as in Fig. 2. The solid orange line is the best-fitting line found using a second-order polynomial, and the shaded area is the $\pm 1\sigma$ zone.

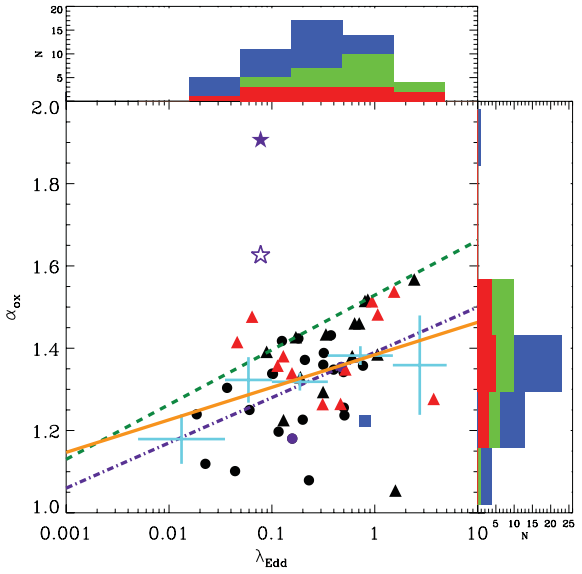

Figure 5. λ_{Edd} versus α_{ox}. Each symbol represents the same type of source as in Fig. 2. The solid orange line is the bisector regression line determined by our sample. The cyan crosses are the binned data points of our sample. The dashed green line is from Lusso10; the dot–dashed purple line is from Grupe10.

especially for the narrow-line objects (the average $\kappa_{2-10\,\mathrm{keV}}$ for our 12 NLS1s is 86^{+96}_{-45}). Lusso10 constructed their broad-band SEDs by first assuming a power law extending from the optical to 500 Å, then connecting the continuum at 500 Å linearly to that at 1 keV and finally by extrapolating from 1 keV towards higher energies, using an exponentially cut-off power law. This model substantially underestimates L_{bol} for narrow-line objects because such objects often have strong soft-X-ray excesses which contain a large fraction of L_{bol} (Jin et al. 2009; Middleton et al. 2009; Paper I). Our detailed broad-band SED fitting has modelled this soft-excess feature by including a low-temperature optically thick Comptonization component. We claim that this results in a more accurate estimate of L_{bol} (Paper I). Therefore, certainly for the nearby type 1 AGNs (redshift <0.4), the $\kappa_{2-10\,\mathrm{keV}}$ versus α_{ox} correlation we find should be more reliable. How the correlation behaves at high redshift requires further study, but Lusso10 has shown that such a second-order polynomial correlation still holds for type 1 AGNs up to redshifts $z = 4$.

3.2.2 *The α_{ox} versus λ_{Edd} correlation*

The existence of a correlation of α_{ox} with λ_{Edd} remains unclear. VF07 found no correlation between these quantities, and so they proposed that α_{ox} did not provide useful information on the broad-band SED shape. S08 confirmed VF07's result for their sample of 35 moderate- to high-luminosity RQ AGNs. On the contrary, Lusso10 did find a correlation between α_{ox} and λ_{Edd}, although with a large dispersion. This was confirmed by Grupe10 for their sample containing 92 soft X-ray selected AGNs, but their correlation was both flatter and stronger than that of Lusso10. We use our sample to investigate this situation, and our results are shown in Fig. 5. The Spearman's rank test gives $\rho_{\mathrm{s}} = 0.35$ and $d_{\mathrm{s}} = 1 \times 10^{-2}$, suggesting that a correlation does exist. We then applied the ordinary least-squares (OLS) regression, assuming λ_{Edd} to be the independent variable, and found the following relation:

$$\alpha_{\mathrm{ox}} = (0.079 \pm 0.038)\log(\lambda_{\mathrm{Edd}}) + (1.384 \pm 0.029). \quad (5)$$

In Fig. 5 we show our results. Our correlation has less dispersion than found by VF07 and Lusso10, but has larger dispersion than that from Grupe10. The exclusion of a correlation is at the $\sim 2\sigma$ significance level, which is less significant than in Grupe10. Our regression line slope is consistent with, but slightly flatter, than that in Lusso10 ($\beta = 0.133 \pm 0.023$) and Grupe10 ($\beta = 0.11 \pm 0.02$). This is partly because our estimation of L_{bol} is higher than in previous studies, due to the inclusion of a soft X-ray excess in our model. Therefore, our value of λ_{Edd} is also higher for the NLS1s and other relatively narrow line objects. Another reason could be a selection effect. We have shown in the previous section that α_{ox} has a luminosity dependence; thus at higher redshift we tend to detect more luminous sources with steeper α_{ox}. While both our sample and that of Grupe10 have low redshifts (this work: $z < 0.4$; Grupe10: $z < 0.3$), Lusso10's sample covers a much larger range in redshift ($0.04 < z < 4.25$), and indeed Lusso10's sample contains many objects with $\alpha_{\mathrm{ox}} > 1.5$ and $z > 0.4$, which populate the empty region above $\alpha_{\mathrm{ox}} = 1.5$ in Fig. 5, and create a larger dispersion. The large dispersion observed in our study and previous work suggests that one should be cautious about using the α_{ox} versus λ_{Edd} relation, because λ_{Edd} inferred by α_{ox} may contain considerable uncertainties.

3.2.3 *The $\kappa_{2-10\,keV}$ versus λ_{Edd} correlation*

Wang et al. (2004) reported the correlation between $\kappa_{2-10\,\mathrm{keV}}$ and λ_{Edd}, which was later confirmed by VF07 and VF09. Most recently, Lusso10 also found this correlation for the 545 X-ray selected type 1 AGNs from the *XMM*–COSMOS survey. They suggested that the observed step change in this correlation does not result from the L_{bol} dependence on both $\kappa_{2-10\,\mathrm{keV}}$ and λ_{Edd}. In our study we also find that λ_{Edd} is correlated with $\kappa_{2-10\,\mathrm{keV}}$. A Spearman's rank test resulted in $\rho_{\mathrm{s}} = 0.60$ and $d_{\mathrm{s}} = 5 \times 10^{-6}$ for the whole sample, and $\rho_{\mathrm{s}} = 0.60$ and $d_{\mathrm{s}} = 5 \times 10^{-6}$ for the 12 NLS1s. Fig. 6 shows our results, together with the results from VF07 and VF09 and Lusso10. We performed an EM regression analysis and derived the following equations.

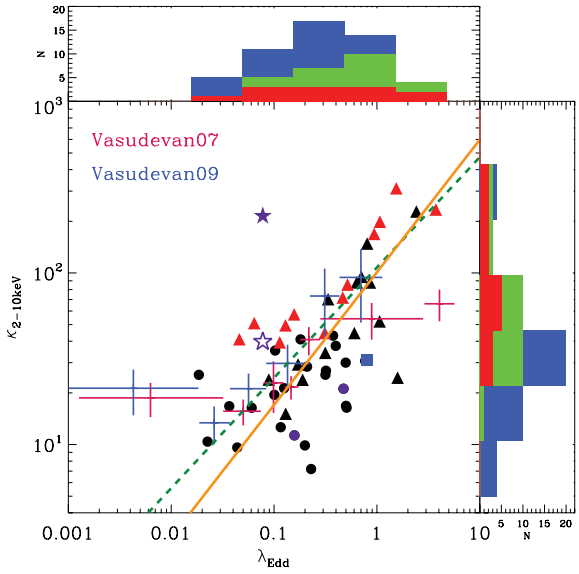

Figure 6. $\lambda_{\rm Edd}$ versus $\kappa_{2-10\,\rm keV}$. Each symbol represents the same type of source as in Fig. 2. The solid orange line is the bisector regression line determined for our sample. The binned data points are from VF07 (pink) and VF09 (blue). The dashed green line is from Lusso10.

(i) An EM regression with $\lambda_{\rm Edd}$ being the independent variable:

$$\log(\kappa_{2-10}) = (0.482 \pm 0.088)\log(\lambda_{\rm Edd}) + (1.840 \pm 0.071). \quad (6)$$

(ii) An EM regression with $\kappa_{2-10\,\rm keV}$ being the independent variable:

$$\log(\kappa_{2-10}) = (1.179 \pm 0.166)\log(\lambda_{\rm Edd}) + (2.232 \pm 0.090). \quad (7)$$

(iii) Bisector of the above two lines (solid orange line in Fig. 6):

$$\log(\kappa_{2-10}) = (0.773 \pm 0.069)\log(\lambda_{\rm Edd}) + (2.004 \pm 0.049). \quad (8)$$

Our regression lines are highly consistent with the binned points from VF07 and VF09 and also with the regression line reported by Lusso10. The two lowest data bins from VF07 and VF09 seem to have a relatively high deviation from the correlation lines, which may imply a change in slope of the correlation for sources with $\lambda_{\rm Edd} < 0.01$. However, we cannot test this possibility from our data due to the exclusion of sources with low $\lambda_{\rm Edd}$ resulting from our sample selection (Paper I).

The results show that the $\kappa_{2-10\,\rm keV}$ versus $\lambda_{\rm Edd}$ correlation extends up to high $\kappa_{2-10\,\rm keV}$ ($\sim$100) and super-Eddington accretion rates ($\sim$10); such objects are mainly NLS1s (red square symbols in Fig. 6) and some other relatively narrow line sources (black square symbols). We also note that the dispersion in our regression line is smaller than that in VF07, VF09 and Lusso10, in spite of the different methods used in deriving $L_{\rm bol}$ and the different redshift ranges. This suggests that the dispersion observed in the correlation is intrinsic. In Fig. 6, we see that PG 1004+130 (filled purple star) deviates far from the regression line (also more than 3σ from the binned data points of VF07 and VF09), confirming its anomalously weak $L_{2-10\,\rm keV}$. Increasing its $L_{2-10\,\rm keV}$ by 0.73 dex (open purple star) moves it much closer to the correlation line.

3.3 Group 3: κ_{5100}, $\lambda_{\rm Eddr}$ and $\kappa_{2-10\,\rm keV}$

The 5100-Å monochromatic continuum luminosity (L_{5100}) is often used to estimate $L_{\rm bol}$, particularly for very large samples of AGNs, when broad-band SED modelling for every source is not practical. The conventional method is to use a constant scaling factor $\kappa_{5100} = 9$ (Kaspi et al. 2000; Richards et al. 2006: 10.3 ± 2.1) or a κ_{5100} value that is anticorrelated with $L_{\rm bol}$ (Marconi et al. 2004, hereafter Marconi04). VF07 showed that for high $\lambda_{\rm Edd}$ sources such as many of the NLS1s, there is a clear deviation from constant $\kappa_{5100} = 9$. In addition, potential contamination from the host galaxy will introduce dispersion into the κ_{5100} versus $\lambda_{\rm Edd}$ correlation for low-luminosity sources. However, this should not be a severe problem for our sample since in our sample host galaxy is not dominating (Paper I). In our study a much stronger correlation was found in κ_{5100} versus $\lambda_{\rm Edd}$ as the Spearman's rank test gives $\rho_{\rm s} = 0.81$ ($d_{\rm s} = 4 \times 10^{-13}$). Motivated by the strong correlations between $\lambda_{\rm Edd}$ and $\kappa_{2-10\,\rm keV}$, we also found a strong correlation between κ_{5100} and $\kappa_{2-10\,\rm keV}$, with a Spearman's rank test of $\rho_{\rm s} = 0.64$ ($d_{\rm s} = 9 \times 10^{-7}$).

The left-hand panel of Fig. 7 shows the correlation between κ_{5100} and $\lambda_{\rm Edd}$. The solid orange line is the OLS regression line, the two dashed orange lines show the $\pm 1\sigma$ region and the shaded region is the $\pm 2\sigma$ region. For a specific $\lambda_{\rm Edd}$ value, the 1σ dispersion of κ_{5100} is $\sim$0.17 dex. The binned data points from VF07 are also shown in the plot for comparison. The VF07 results are consistent with ours within $\pm 2\sigma$, but our correlation is much stronger. This may be attributed to the high spectral quality of our sample and the carefully derived κ_{5100} and $\lambda_{\rm Edd}$ correlation, based on our detailed broad-band SED fitting. It also shows that the distribution of κ_{5100} peaks at 10–20, with a 1σ dispersion of 0.29 dex. For the NLS1s, the mean κ_{5100} increases to 20 ($1\sigma = 0.23$ dex). This means that using $\kappa_{5100} = 9$ (the horizontal purple line in the left-hand panel of Fig. 7) would underestimate the intrinsic $L_{\rm bol}$ and $\lambda_{\rm Edd}$, especially for samples containing sources with high $\lambda_{\rm Edd}$, e.g. the NLS1s. The OLS regression line that assumes $\lambda_{\rm Edd}$ to be the independent variable can be expressed by the following equation:

$$\log(\kappa_{5100}) = (0.467 \pm 0.045)\log(\lambda_{\rm Edd}) + (1.430 \pm 0.027). \quad (9)$$

We superimpose the SDSS and FAST (Landt et al. 2011) data from Mrk 110 (filled and open green square, respectively) on Fig. 7. This shows the large optical variability in the spectrum. The FAST data are much more consistent with the *XMM–Newton* OM and also matches very well with the regression line. This supports the reliability of the correlation.

The strong correlation between κ_{5100} and $\kappa_{2-10\,\rm keV}$ (shown in the right-hand panel of Fig. 7) is an expected result, given that both κ_{5100} and $\kappa_{2-10\,\rm keV}$ strongly correlate with $\lambda_{\rm Edd}$. Such a correlation is also reasonable considering the strong correlation between $L_{2-10\,\rm keV}$ and L_{5100} (Paper II). The 1σ dispersion of $\kappa_{2-10\,\rm keV}$ is 0.40 dex, which is larger than that for κ_{5100}, 0.29 dex. The $\pm 1\sigma$ and $\pm 2\sigma$ zones are also shown in the figure. The bisector regression line can be expressed by the following equation:

$$\log(\kappa_{5100}) = (0.593 \pm 0.053)\log(\kappa_{210}) + (0.239 \pm 0.086). \quad (10)$$

Mrk 110 and PG 1004+130 are superimposed on the plot, and their corrected positions are much more consistent with the regression lines.

Marconi04 proposed that κ_{5100} anticorrelated with $L_{\rm bol}$, but our study does not support such an anticorrelation, although our sample only occupies the $L_{\rm bol}$ region above $10^{10.7}\,{\rm L}_{\odot}$ in fig. 3 left-hand panel of Marconi04. A Spearman's rank test for our sample gives $\rho_{\rm s} = 0.12$ ($d_{\rm s} = 0.39$), suggesting no correlation. The sources lying between 10^{11} and $10^{12.5}\,{\rm L}_{\odot}$ have a mean $\kappa_{5100} = 16$, with a 1σ dispersion of 0.29 dex. Therefore, we find that our κ_{5100} values for these objects are much higher than reported in Elvis et al. (1994) and Marconi04.

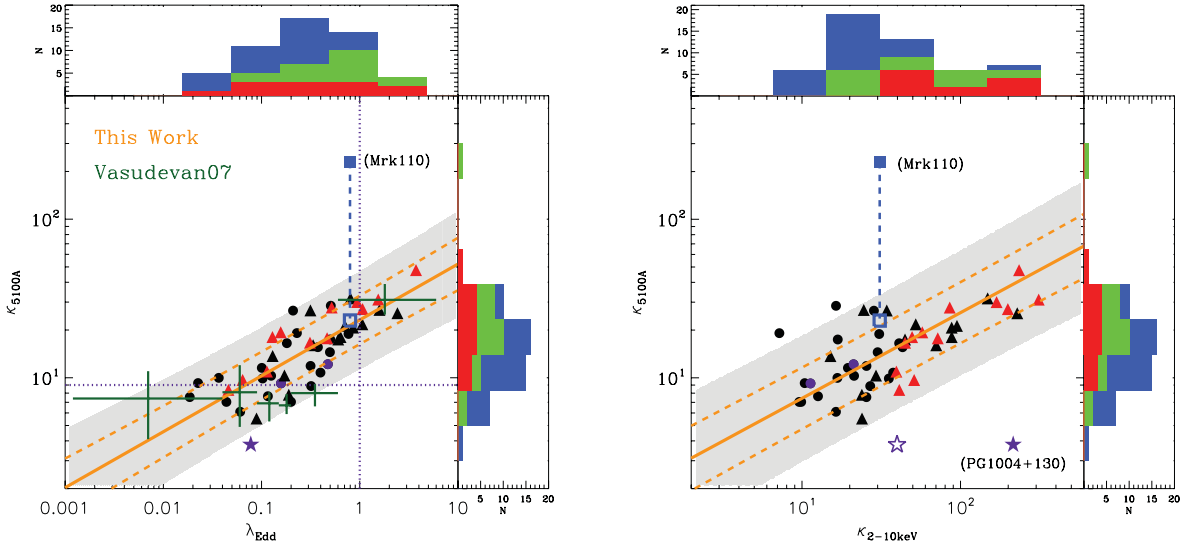

Figure 7. κ_{5100} versus $\lambda_{\rm Edd}$ and $\kappa_{2-10\,\rm keV}$. Each symbol represent the same type of source as in Fig. 2. In the left-hand panel, the solid orange line is the OLS line assuming $\lambda_{\rm Edd}$ to be the independent variable. The two dashed orange lines show the $\pm1\sigma$ region, and the shaded region is the $\pm2\sigma$ region. The blue open square symbol is Mrk 110 reported by Landt et al. (2011), which is connected by the blue dashed line to the filled blue square point measured from SDSS spectrum. The vertical and horizontal purple lines are for $\kappa_{5100} = 9$ and $\lambda_{\rm Edd} = 1$. The symbols and lines in the right-hand panel have the same meaning as those in the left-hand panel.

3.4 Group 4: $\Gamma_{2-10\,\rm keV}$, $\lambda_{\rm Edd}$ and $\kappa_{2-10\,\rm keV}$

The strong correlation between 2–10 keV photon index ($\Gamma_{2-10\,\rm keV}$) and $\lambda_{\rm Edd}$ has been studied in detail for the past 10 years (e.g. Lu & Yu 1999; Wang et al. 2004; S06; S08; Zhou10a; Trump et al. 2011). It is proposed that increasing the mass accretion rate leads to enhanced emission from the accretion disc, resulting in more seed photons from the disc, which then increases the Compton cooling of the corona, and softens the Comptonized hard X-ray spectrum, i.e. the slope of $\Gamma_{2-10\,\rm keV}$ increases. It was also reported that both $\Gamma_{2-10\,\rm keV}$ and $\lambda_{\rm Edd}$ strongly correlate with the FWHM of Hβ (e.g. Brandt, Mathur & Elvis 1997; S06; S08; Grupe10); therefore, these three parameters all strongly correlate with each other. However, S06 and S08 found that the correlation of $\Gamma_{2-10\,\rm keV}$ with $\rm FWHM_{H\beta}$ is weakened by the inclusion of highly luminous sources, but that the correlation of $\Gamma_{2-10\,\rm keV}$ with $\lambda_{\rm Edd}$ still exists. This implies that the correlation of $\Gamma_{2-10\,\rm keV}$ with $\lambda_{\rm Edd}$ is more fundamental. We also mentioned in Section 3.2 that the strong correlation between $\lambda_{\rm Edd}$ and $\kappa_{2-10\,\rm keV}$ is confirmed; thus a strong correlation between $\Gamma_{2-10\,\rm keV}$ and $\kappa_{2-10\,\rm keV}$ is expected. Indeed, such a correlation has been reported recently by Zhou & Zhao (2010b, hereafter Zhou10b). In this section we carry out a similar cross-correlation study to test the robustness of previous claims.

3.4.1 *The correlations and regression lines*

The two panels in Fig. 8 show our correlations between $\Gamma_{2-10\,\rm keV}$, $\lambda_{\rm Edd}$ and $\kappa_{2-10\,\rm keV}$. Table 3 summarizes the numerical results.

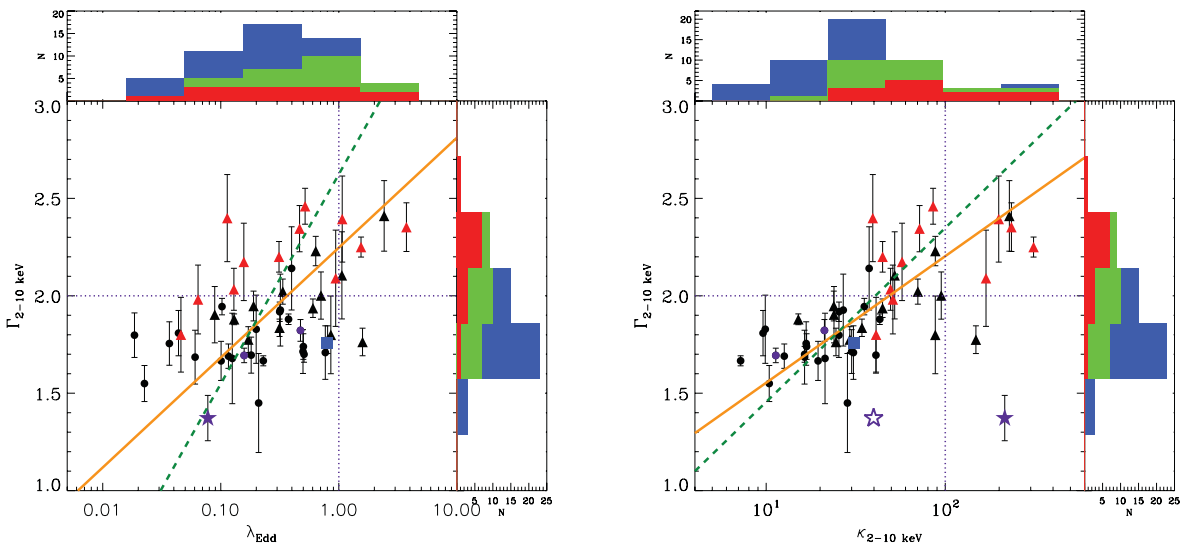

Figure 8. $\Gamma_{2-10\,\rm keV}$ versus $\lambda_{\rm Edd}$ and $\kappa_{2-10\,\rm keV}$. Each symbol represents the same type of source as in Fig. 2. In the left-hand panel, the solid orange line is the bisector regression line. The dashed green line is that reported by Zhou10b. The vertical and horizontal purple lines are for $\Gamma_{2-10\,\rm keV} = 2$ and $\lambda_{\rm Edd} = 1$. The symbols and lines in the right-hand panel have the same meaning as those in the left-hand panel. The vertical purple line is for $\kappa_{2-10\,\rm keV} = 100$.

Table 3. The line coefficients found using different regression methods for the correlations of $\Gamma_{2-10\,\mathrm{keV}}$ versus λ_{Edd} and $\kappa_{2-10\,\mathrm{keV}}$.

		$\log(\lambda_{\mathrm{Edd}}) = \beta\Gamma+\xi$	$\log(\kappa_{210}) = \beta\Gamma+\xi$
OLS($Y\|X$)	β	0.918 ± 0.269	1.115 ± 0.172
	ξ	-2.325 ± 0.527	-0.573 ± 0.329
OLS($X\|Y$)	β	4.730 ± 1.217	2.209 ± 0.283
	ξ	-9.650 ± 2.304	-2.675 ± 0.525
Bisector	β	1.753 ± 0.239	1.533 ± 0.153
	ξ	-3.931 ± 0.471	-1.376 ± 0.288
χ^2 min	β	4.416 ± 0.510	2.620 ± 0.184
	ξ	-8.761 ± 0.946	-3.447 ± 0.343
$\chi^2/\nu \sim 1$	β	1.274 ± 0.283	1.529 ± 0.183
	ξ	-3.003 ± 0.544	-1.372 ± 0.350

Significant correlations are confirmed based on the Spearman's rank test: $\rho_s = 0.40$ ($d_s = 4 \times 10^{-3}$) for $\Gamma_{2-10\,\mathrm{keV}}$ versus λ_{Edd} and $\rho_s = 0.73$ ($d_s = 4 \times 10^{-9}$) for $\Gamma_{2-10\,\mathrm{keV}}$ versus $\kappa_{2-10\,\mathrm{keV}}$.

Following S08's approach, we applied the χ^2 minimization method for $\Gamma_{2-10\,\mathrm{keV}}$ versus λ_{Edd} correlation, assuming $\Gamma_{2-10\,\mathrm{keV}} = \beta\log(\lambda_{\mathrm{Edd}}) + \xi$. A typical error of 10 per cent was assumed for λ_{Edd}. The small error in $\Gamma_{2-10\,\mathrm{keV}}$ for Mrk 110 (the blue square symbol) caused the slope β to be 0.018 ± 0.019, which is clearly not the best-fitting line for the whole sample. We therefore excluded Mrk 110 and so found a more reasonable slope of 0.189 ± 0.026, but this is still $\sim 5\sigma$ away from 0.31 ± 0.01 reported by S08 using the same method. It implies that the χ^2 minimization technique may not be an appropriate method for quantifying this correlation, because it can be strongly biased by sources with small error in the $\Gamma_{2-10\,\mathrm{keV}}$ measurement (if the 2–10 keV spectrum has high S/N). The $\chi^2/\nu = 6.5$ in our fitting means that this correlation contains a big intrinsic dispersion along with the observational dispersion; thus the method of assuming $\chi^2/\nu \sim 1$ by taking intrinsic dispersion into account is more appropriate. This method gives slopes of 0.202 ± 0.061 and 0.226 ± 0.026 before and after excluding Mrk 110, so the results are less sensitive to individual sources of much smaller error bars. The intrinsic dispersion is 0.18, which is 86 per cent of the total dispersion, and is also consistent with $\Delta\Gamma_{2-10\,\mathrm{keV}} \sim 0.1 \times \Gamma_{2-10\,\mathrm{keV}}$ reported in S08. The bisector regression line is derived. The result is plotted as a solid orange line in the left-hand panel of Fig. 8, and it can be expressed by the following equation:

$$\log(\lambda_{\mathrm{Edd}}) = (1.773 \pm 0.238)\Gamma_{2-10\,\mathrm{keV}} - (3.983 \pm 0.469). \quad (11)$$

The slope is $\sim 2\sigma$ steeper than the bisector slope of 0.9 ± 0.3 reported by S08 (dashed green line in the left-hand panel of Fig. 8). This discrepancy may be due to the different methods used to estimate the bolometric luminosity. We will discuss this point in Section 3.4.2.

Similar analytical methods were applied to the relation of $\Gamma_{2-10\,\mathrm{keV}}$ versus $\kappa_{2-10\,\mathrm{keV}}$. Zhou10b reported a slope of 2.52 ± 0.08 using standard χ^2 minimization and assuming $\kappa_{2-10\,\mathrm{keV}} = \beta\log(\Gamma_{2-10\,\mathrm{keV}}) + \xi$. This is consistent with our value of $\beta = 2.620 \pm 0.184$ with a $\chi^2/\nu = 2.78$. Considering the intrinsic scatter, Zhou10b reported a slope of 1.12 ± 0.30 by adding 0.32 dex of intrinsic dispersion to reduce χ^2/ν to unity (the dashed green line in the right-hand panel of Fig. 8). Applying the same method to our sample resulted in a slope of 1.529 ± 0.183, which is steeper than found by Zhou10b. The intrinsic dispersion found by us is 80 per cent of the total dispersion. The bisector regression method gives a slope of 1.533 ± 0.153 (the solid orange line in the right-hand panel of Fig. 8) and can be expressed by the following equation:

$$\log(\kappa_{2-10\,\mathrm{keV}}) = (1.533 \pm 0.153)\Gamma - (1.376 \pm 0.288). \quad (12)$$

This is also consistent with the results found by assuming $\chi^2/\nu \sim 1$.

3.4.2 Advances from our correlation analysis

Compared with the results found by S08 and Zhou10b, our study of $\Gamma_{2-10\,\mathrm{keV}}$ versus λ_{Edd} and $\Gamma_{2-10\,\mathrm{keV}}$ versus $\kappa_{2-10\,\mathrm{keV}}$ provides the following advances.

(1) We have confirmed these correlations based on a sample twice the size of those in S08 and Zhou10b, including more sources with high values of λ_{Edd}, $\Gamma_{2-10\,\mathrm{keV}}$ and $\kappa_{2-10\,\mathrm{keV}}$, which significantly extend the previous correlations (see Fig. 8). The regression line fits are better constrained and cover wider parameter space. The difference between our regression lines and those of previous studies may be partially due to the fact that we have more sources of most extreme λ_{Edd}.

(2) Our sample has been carefully screened to exclude sources with a strong warm absorber. These sources may have artificially lower $\Gamma_{2-10\,\mathrm{keV}}$ and higher $\kappa_{2-10\,\mathrm{keV}}$ than the intrinsic values. Our sample quality is essential to reduce the dispersion and so reveal intrinsic correlations.

(3) Our estimates of L_{bol} were derived from the broad-band SED fitting, which was based on high-quality spectra and a new multicomponent model. We claim this to be more reliable than the procedure used in previous studies. A conventional method is to apply a multiplication factor to L_{5100} to estimate L_{bol}. However, we showed in Section 3.3 that κ_{5100} is well correlated with λ_{Edd}, rather than being constant or dependent on L_{bol}; consequently, the conventional scaling from L_{5100} to L_{bol} is likely to result in poor accuracy in some cases. The L_{bol} used in Zhou10b does come from VF09's broad-band SED model for the reverberation mapped sample, but it does not take account of the 'soft X-ray excess' component or where the disc peaks in the EUV. Therefore the L_{bol} we calculate will be larger than previous works, especially for those sources with a strong 'soft excess'. Our λ_{Edd} and $\kappa_{2-10\,\mathrm{keV}}$ will also be higher, which could account for the differences in slope between our regression lines and those reported in previous work.

3.5 Group 5: $\Gamma_{2-10\,\mathrm{keV}}$, H$\beta$ FWHM and M_{BH}

3.5.1 The $\Gamma_{2-10\,keV}$ versus Hβ FWHM correlation

The correlations between the soft/hard X-ray slopes and the Balmer line velocity width have been the subject of many previous studies. Puchnarewicz et al. (1992) studied 53 AGNs with ultrasoft X-ray excess and noted that these ultrasoft AGNs tend to have narrower optical permitted lines. Laor et al. (1994) studied 23 *ROSAT* selected bright quasars, and found an anticorrelation between the 0.2–2 keV slope (α_{X}) and the Hβ line width. Later Boller et al. (1996) showed that NLS1s tend to have softer X-ray spectra. Brandt et al. (1997) extended this anticorrelation to include the 2–10 keV slope by showing that NLS1s also have steeper hard X-ray continua than BLS1s, a result which was confirmed and extended by other studies (e.g. Grupe et al. 1999; Leighly 1999; Piconcelli et al. 2005; Brocksopp et al. 2006; S08; Zhou10a). However, there is large scatter within this correlation, and the trend seems to invert below $\sim 1000\,\mathrm{km\,s^{-1}}$ for NLS1s (Zhou et al. 2006). The observed large scatter is to be expected since we know that it is not a single variable that determines the spectral slope in either the soft or the hard X-ray region. In the

soft X-ray region, the extinction, a soft-excess component and a warm absorber will all influence the spectral shape, which would require very detailed modelling. The situation for the 2–10 keV region is somewhat less complicated since often a single power law dominates (e.g. Middleton et al. 2007), but a warm absorber and reflection may still modify the hard X-ray spectral shape. In summary, the true correlation can only be found when the intrinsic X-ray continuum is used.

Our sample selection has ensured that every object in the sample has high-quality 2–10 keV spectra, without significant cold gas absorption or a warm absorber (Paper I). We confirm that there is an anticorrelation between $\Gamma_{2-10\,\mathrm{keV}}$ and Hβ FWHM (see Fig. 9). The Spearman's rank test gives $\rho_s = -0.72$ ($d_s = 4.9 \times 10^{-9}$). The best-fitting lines from Zhou10a are also plotted in Fig. 9 as the cyan lines. Compared with their linear correlation in using $\mathrm{FWHM}_{\mathrm{H}\beta}$, we find that the linear correlation using $\log(\mathrm{FWHM}_{\mathrm{H}\beta})$ is better. Previous work also noted that the correlation may change form at $\sim$4000 km s^{-1} (Sulentic et al. 2008). Therefore we fit a broken power law to the data points in the left-hand panel by assuming a break point at $\mathrm{FWHM}_{\mathrm{H}\beta} = 4000\,\mathrm{km\,s^{-1}}$. Intrinsic dispersion will dominate this correlation as shown in previous studies (e.g. Grupe et al. 1999; Grupe10; Zhou10a), so we performed this fitting without considering the error in $\Gamma_{2-10\,\mathrm{keV}}$ associated with each point; otherwise, the fitting would be biased by the few points with best constrained $\Gamma_{2-10\,\mathrm{keV}}$ rather than revealing the distribution of the whole sample. The best-fitting parameters are shown below:

(i) when $\mathrm{FWHM}_{\mathrm{H}\beta} \leq 4000\,\mathrm{km\,s^{-1}}$,

$$\Gamma = (-0.86 \pm 0.01)\log(\mathrm{FWHM}_{\mathrm{H}\beta}) + (4.89 \pm 0.03); \quad (13)$$

(ii) when $\mathrm{FWHM}_{\mathrm{H}\beta} > 4000\,\mathrm{km\,s^{-1}}$,

$$\Gamma = (-0.11 \pm 0.01)\log(\mathrm{FWHM}_{\mathrm{H}\beta}) + (2.20 \pm 0.04). \quad (14)$$

Sources with $\mathrm{FWHM}_{\mathrm{H}\beta} > 4000\,\mathrm{km\,s^{-1}}$ have an average $\Gamma_{2-10\,\mathrm{keV}} = 1.78 \pm 0.12$. The only source included in the correlation

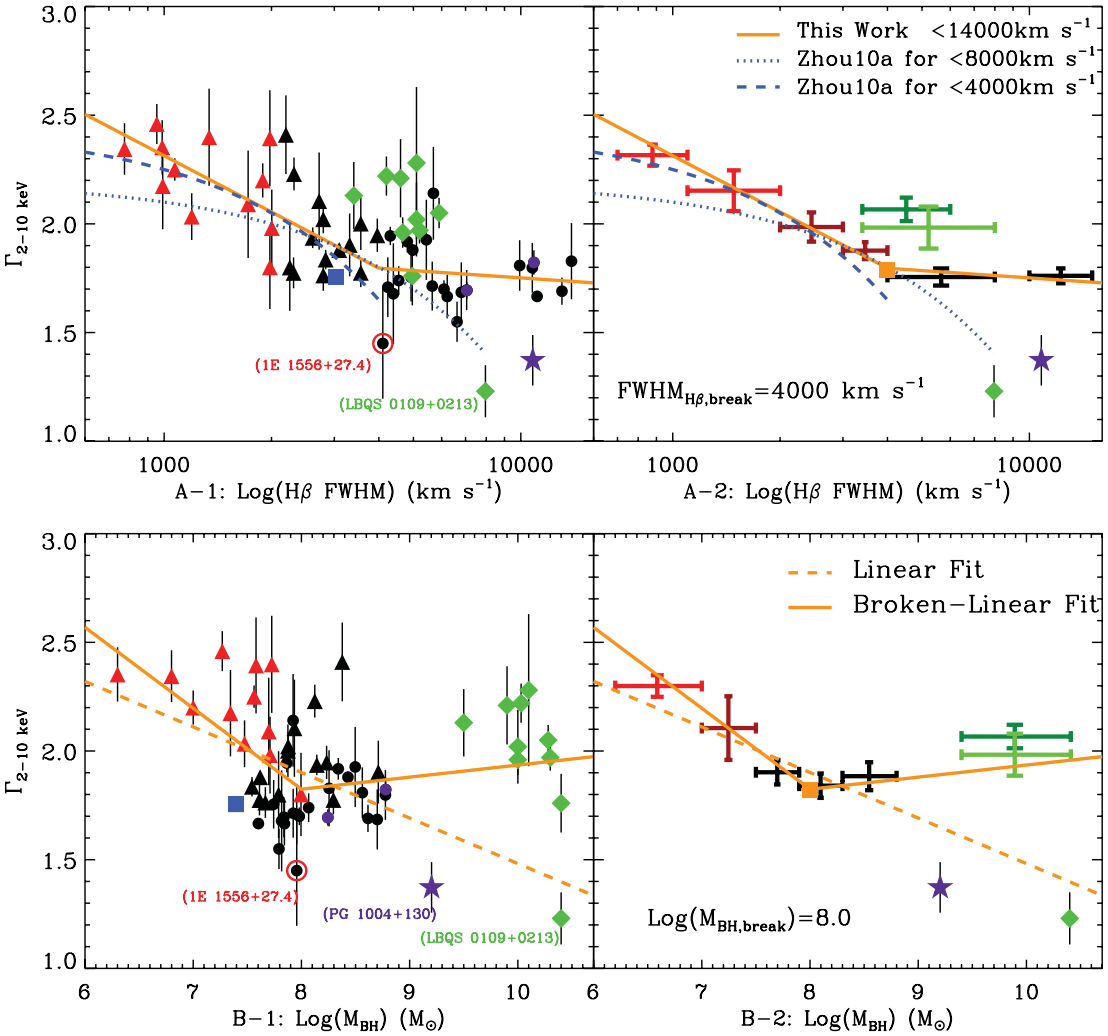

Figure 9. $\Gamma_{2-10\,\mathrm{keV}}$ versus FWHM of Hβ and M_{BH}. In the upper-left panel, a broken line is fitted to the sample using the minimum χ^2 method, with the break point chosen to be FWHM = 4000 km s^{-1} (the orange square point). S06 and S08 proposed the linear correlation between $\Gamma_{2-10\,\mathrm{keV}}$ and log(Hβ FWHM) was not followed by their 10 extremely high luminosity sources, so we plot their sample as blue diamond symbols for comparison. In the right-hand panel, binned points are plotted with 1 standard error of $\Gamma_{2-10\,\mathrm{keV}}$ in order to show the break points more clearly. The two red points only include the NLS1s, while the two dark points are the broadest BLS1s. The cyan point is the binned point for the whole sample of S06 and S08. The blue point is the binned point for the sample of S06 and S08 but excluding LBQS 0109+0213 whose $\Gamma_{2-10\,\mathrm{keV}}$ is anomalously low. 1E 1556+27.4 shown by the red circle is another source with $\Gamma_{2-10\,\mathrm{keV}} < 1.5$. In the second row, all the symbols have the same meaning as in the first row; the break point is chosen to be $\log(M_{\mathrm{BH}}) = 8.0$ (the orange square point). We plot the linear regression line as the dashed orange line.

whose $\Gamma_{2-10\,\mathrm{keV}} < 1.5$ is 1E 1556+27.4 (the data for PG 1004+130 are superimposed but not used for the regression). A closer examination of the spectrum of this AGN shows that it probably has a strong reflection component modifying its intrinsic hard X-ray power-law slope (Paper I). All other objects have values consistent with $\Gamma_{2-10\,\mathrm{keV}} > 1.5$. The differences in the results of Zhou10a and our work are not only because we performed our correlation fitting using $\log(\mathrm{FWHM}_{\mathrm{H}\beta})$, but also because their sample did not exclude BAL quasars and warm absorbers, whose low values of $\Gamma_{2-10\,\mathrm{keV}}$ are probably not intrinsic. This will bias the correlation and increase the scatter.

Our sample includes six objects with $\mathrm{FWHM}_{\mathrm{H}\beta} > 10\,000\,\mathrm{km\,s^{-1}}$. These are the sources that have average $\langle\Gamma_{2-10\,\mathrm{keV}}\rangle = 1.76 \pm 0.14$ independent of $\mathrm{FWHM}_{\mathrm{H}\beta}$. This is slightly lower but still consistent with the $\Gamma_{2-10\,\mathrm{keV}} = 1.97 \pm 0.31$ index found by S06 and S08, who included more high-redshift, high-luminosity sources, with $\mathrm{FWHM}_{\mathrm{H}\beta} > 10\,000\,\mathrm{km\,s^{-1}}$.

3.5.2 *The $\Gamma_{2-10\,keV}$ versus M_{BH} correlation*

The Hβ FWHM is frequently used to estimate M_{BH} using the relation $M_{\mathrm{BH}} \propto \mathrm{FWHM}^2_{\mathrm{H}\beta}$ (Wandel, Peterson & Malkan 1999; Woo & Urry 2002). The correlation of $\Gamma_{2-10\,\mathrm{keV}}$ with $\mathrm{FWHM}_{\mathrm{H}\beta}$ implies a similar correlation in $\Gamma_{2-10\,\mathrm{keV}}$ versus M_{BH} (Kelly et al. 2008). This is confirmed in our study as shown in the second row of Fig. 9. The Spearman's rank test gives $\rho_{\mathrm{s}} = -0.3$ ($d_{\mathrm{s}} = 3 \times 10^{-2}$). We also plot $\mathrm{FWHM}_{\mathrm{H}\beta}$ versus M_{BH} in Fig. 10. This is an independent plot as our M_{BH} are derived from the SED continuum fits rather than directly measured from $\mathrm{FWHM}_{\mathrm{H}\beta}$. The OLS regression gives $M_{\mathrm{BH}} \propto \mathrm{FWHM}^{1.16}_{\mathrm{H}\beta}$, with $1\sigma = 0.4$ dex. The cyan triangle symbol in the figure shows the position of the break in $\mathrm{FWHM}_{\mathrm{H}\beta}$ versus M_{BH}. The correlation in Fig. 10 suggests $\mathrm{FWHM}_{\mathrm{H}\beta} = 4000\,\mathrm{km\,s^{-1}}$ corresponds to a black hole mass of $10^8\,\mathrm{M}_\odot$. Indeed, the correlation in the second row of Fig. 9 shows a change in slope at $\log(M_{\mathrm{BH}}) \sim 8.0$. A broken power-law fitting, assuming the break point at $\log(M_{\mathrm{BH}}) = 8.0$, can be expressed as follows:

(i) when $\log(M_{\mathrm{BH}}) \leq 8.0$,

$$\Gamma_{2-10\,\mathrm{keV}} = (-0.372 \pm 0.005)\log(M_{\mathrm{BH}}) + (4.802 \pm 0.037); \quad (15)$$

(ii) when $\log(M_{\mathrm{BH}}) > 8.0$,

$$\Gamma_{2-10\,\mathrm{keV}} = (0.056 \pm 0.007)\log(M_{\mathrm{BH}}) + (1.380 \pm 0.052). \quad (16)$$

Sources with $\log(M_{\mathrm{BH}}) > 8.0$ have an average $\Gamma_{2-10\,\mathrm{keV}} = 1.86 \pm 0.21$.

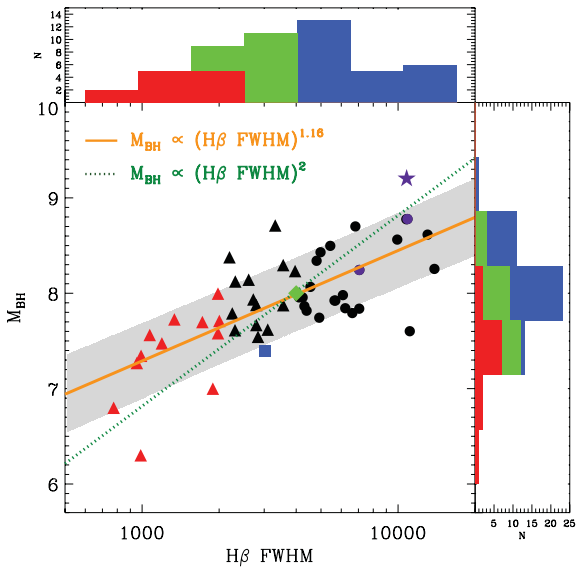

Figure 10. M_{BH} versus Hβ FWHM. Note that the black hole mass M_{BH} was constrained by Hβ FWHM and obtained from the broad-band SED fitting (i.e. the $M_{\mathrm{BH,FIT}}$ in Paper I), rather than directly calculated from the Hβ FWHM. The symbols used represent the different types of source as in Fig. 2. The solid orange line is the OLS regression line, assuming Hβ FWHM to be the independent variable. The shaded region is the $\pm 1\sigma$ region of the regression line. The cyan triangle shows the position of [$\mathrm{FWHM}_{\mathrm{H}\beta,\mathrm{break}}$, $\log(M_{\mathrm{BH,break}})$] in Fig. 9.

3.6 Other strong correlations

The diverse correlations found in small parameter groups imply more correlations among all these parameters. We show some significant correlations in Fig. 11. These include decreasing λ_{Edd}, $\kappa_{2-10\,\mathrm{keV}}$ and κ_{5100} with increasing Hβ FWHM and M_{BH}. Binned data points are shown as cyan crosses. The dashed orange line in each panel is the bisector regression line.

3.6.1 *The $\kappa_{2-10\,keV}$ versus $L_{2-10\,\mathrm{keV}}$ correlation*

Marconi04 and Hopkins07 reported a strong positive correlation in $\kappa_{2-10\,\mathrm{keV}}$ versus $L_{2-10\,\mathrm{keV}}$ based on a quasar SED template and the α_{ox} versus L_{2500} correlation reported by Steffen et al. (2006). VF07 tested the same correlation in their low-redshift AGN sample but found no correlation (see Fig. 12). We tested this correlation in our sample and confirmed VF07's result (see Fig. 12). A highly dispersed anticorrelation of $\kappa_{2-10\,\mathrm{keV}}$ with $L_{2-10\,\mathrm{keV}}$ is found in our study.

For the well-sampled high X-ray luminosity region ($L_{2-10\,\mathrm{keV}} > 10^{43}\,\mathrm{erg\,s^{-1}}$), both the VF07 sample and ours show very similar distribution and dispersion. NLS1s in both samples mainly populate the regions of $\kappa_{2-10\,\mathrm{keV}} \gtrsim 100$ and $10^{42} < L_{2-10\,\mathrm{keV}} < 10^{43}\,\mathrm{erg\,s^{-1}}$, and deviate from the correlation suggested by Marconi04 and Hopkins07. The main difference from VF07 is that our sample has more sources within the range $3 \times 10^{42} < L_{2-10\,\mathrm{keV}} < 10^{43}\,\mathrm{erg\,s^{-1}}$, while VF07 sample contains three extraordinary weak X-ray sources with $L_{2-10\,\mathrm{keV}} < 2 \times 10^{42}\,\mathrm{erg\,s^{-1}}$. Thus we think that those intrinsically X-ray weak ($L_{2-10\,\mathrm{keV}} \sim 10^{42}\,\mathrm{erg\,s^{-1}}$) sources may populate the low $L_{2-10\,\mathrm{keV}}$, small $\kappa_{2-10\,\mathrm{keV}}$ region, creating a totally dispersed distribution in the $\kappa_{2-10\,\mathrm{keV}}$ versus $L_{2-10\,\mathrm{keV}}$ plot. The correlations from Marconi04 and Hopkins07 may have underestimated the uncertainties in using α_{ox} versus L_{2500} correlation (see discussion in Section 3.1) and the universal quasar SED template (e.g. Elvis et al. 1994; VF07; Paper I). However, we cannot rule out the possibility that the behaviours of nearby Seyfert AGNs are different from quasars at higher redshift.

3.6.2 *α_{UV} and α_X related correlations*

While $\Gamma_{2-10\,\mathrm{keV}}$ is the 2–10 keV photon index measured directly from the X-ray data, we can also measure the optical/UV slope and soft X-ray slope from our reconstructed SED. Assuming $F_\nu \propto \nu^{-\alpha}$, we define α_{UV} as the spectral slope between 1700 and 6500 Å (the *Swift* UVOT wavelength coverage), and α_{X} as the soft X-ray slope between 0.2 and 2 keV, so as to be comparable with the results in Grupe10. Note that we do not have complete OM data for every source, and we only use X-ray data from *XMM–Newton*

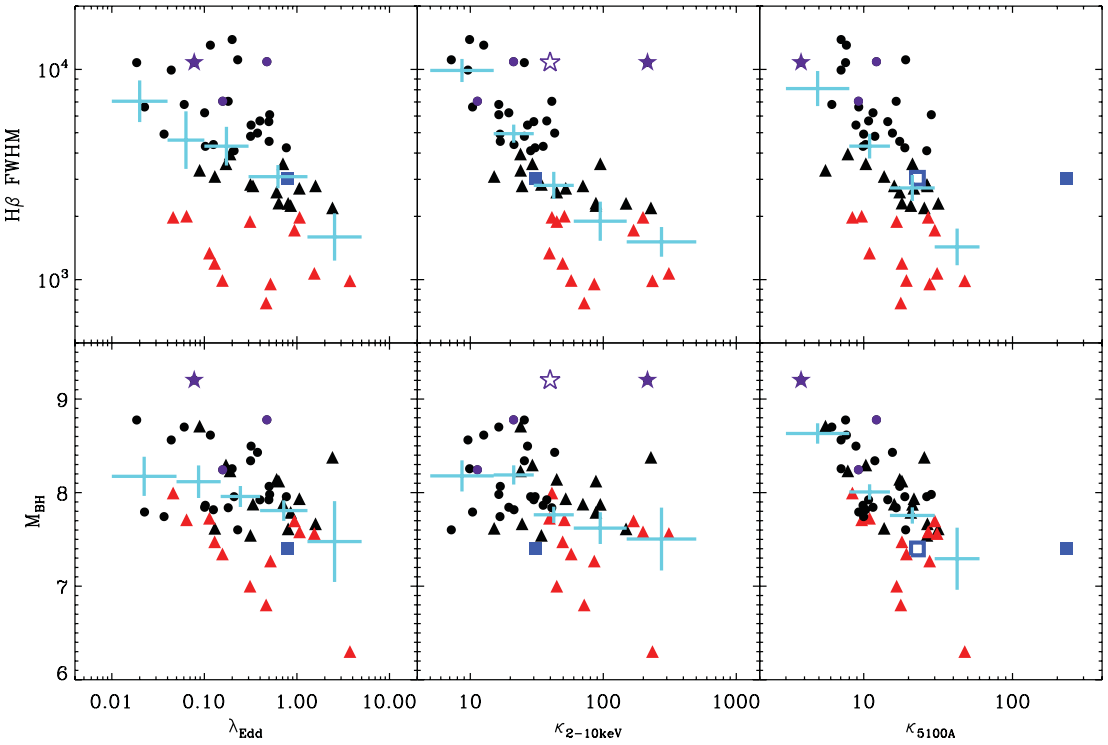

Figure 11. Examples of some good correlations not reported previously. In each panel the various symbols represent the same types of source as in Fig. 2. The cyan symbols are the binned data points over the *X*-axis with 1 standard error on the *Y*-axis.

above 0.3 keV, so our α_{UV} and α_X values are model-dependent. The soft X-ray and optical/UV regions cannot be simply fitted by a single power law (see the SEDs in Paper I), and thus α_{UV} and α_X are just rough estimates of the spectral shape. We measure α_{UV} and α_X from the best-fitting SED in Paper I corrected for Galactic and intrinsic reddening/absorption, and list the values in Table B2.

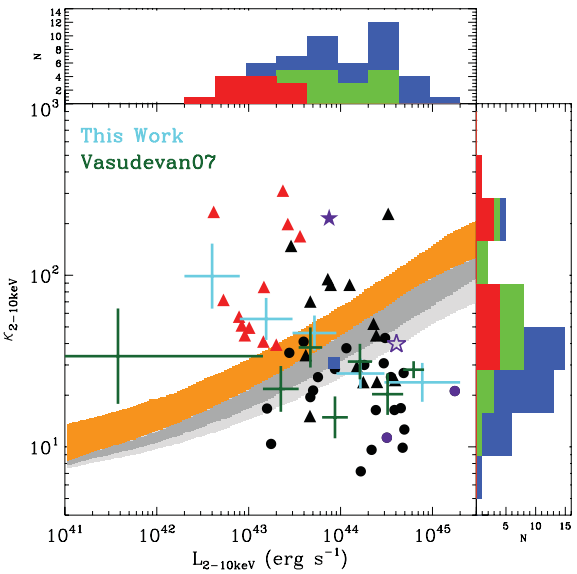

Figure 12. $\kappa_{2-10\,keV}$ versus $L_{2-10\,keV}$. Different symbols represent the same type of sources as in Fig. 2. The orange and grey shaded regions represent the theoretical $\kappa_{2-10\,keV}$ with $\pm1\sigma$ scattering at each $L_{2-10\,keV}$ in Hopkins07 and Marconi04. The green data points are reproduced from Fig. 3 in VF07.

It was found previously that AGNs with bluer optical/UV spectra tend to have softer X-ray spectra (Walter & Fink 1993; Grupe et al. 1998; Grupe10). We found $\rho_s = -0.65$ ($d_s = 4 \times 10^{-7}$) for α_{UV} versus $\Gamma_{2-10\,keV}$ and $\rho_s = -0.41$ ($d_s = 3 \times 10^{-3}$) for α_{UV} versus α_X, so confirm the results from other studies. We also tested the results of α_{UV} and α_X without correction for intrinsic reddening/absorption. The Spearman's rank coefficients remain similar, which is because of the unobscured nature of our sample. Another correlation found in previous work is that AGNs with steeper X-ray spectra tend to be weak at hard X-ray energies (Atlee & Mathur 2009; Grupe10; but see also Young, Elvis & Risaliti 2009). This can be directly confirmed in our study by the anticorrelation found between α_X and $L_{2-10\,keV}$ ($\rho_s = -0.60$ and $d_s = 6 \times 10^{-6}$) and the correlation between α_X and α_{ox} ($\rho_s = 0.65$ and $d_s = 5 \times 10^{-7}$; Fig. 13). However, we only find a marginal anticorrelation between α_{UV} and α_{ox} (see Table 4), which is much less significant than that found by Grupe10. This seems to be due to the fact that our sample has few sources with $\alpha_{ox} > 1.6$ and $\alpha_{UV} < 0$.

Similar to the $\Gamma_{2-10\,keV}$ versus λ_{Edd} correlation discussed in Section 3.4, α_X and α_{UV} were also found to (anti)correlate with λ_{Edd} (Grupe 2004; S08; Grupe10). This is confirmed in our study as we find $\rho_s = 0.49$ ($d_s = 4 \times 10^{-4}$) for α_X versus λ_{Edd} which is stronger than the correlation between $\Gamma_{2-10\,keV}$ and λ_{Edd}, and $\rho_s = -0.55$ ($d_s = 4 \times 10^{-5}$) for α_{UV} versus λ_{Edd}. In addition, we also find strong (anti)correlations such as α_X (or α_{UV}) versus $\kappa_{2-10\,keV}$, α_X (or α_{UV}) versus $\kappa_{5100\,Å}$, α_X (or α_{UV}) versus $FWHM_{H\beta}$ and α_X (or α_{UV}) versus M_{BH} (see Fig. 13 and Table 4).

4 A SYSTEMATIC CORRELATION STUDY ON THE KEY PARAMETERS

To summarize the various correlations discussed in the previous section, we performed a systematic correlation study of the

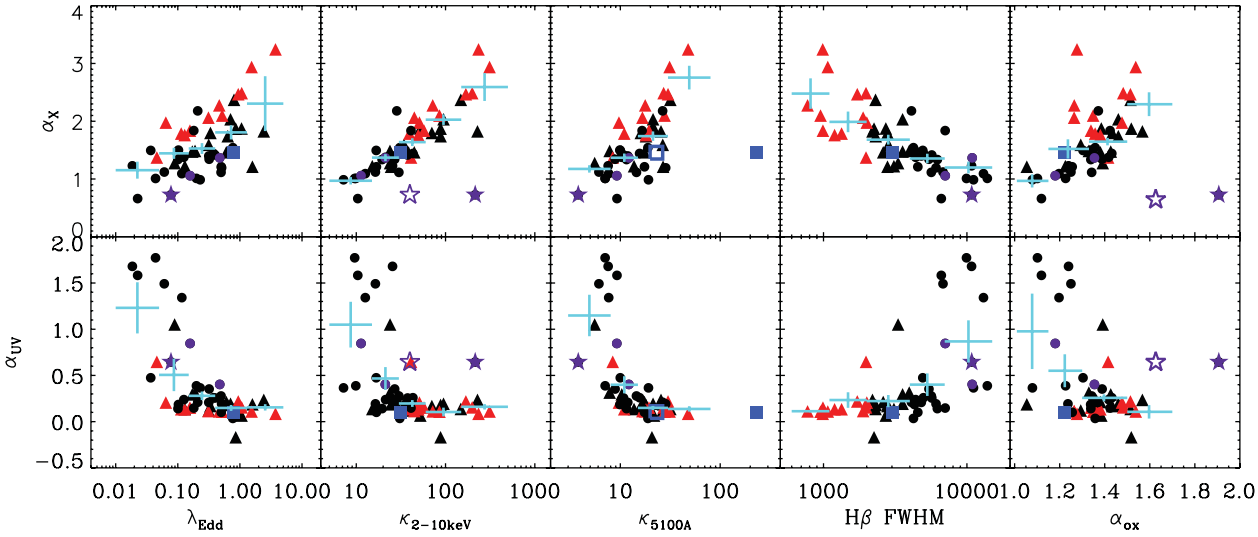

Figure 13. Examples of some good correlations not reported previously. In each panel the various symbols represent the same types of source as in Fig. 2. The cyan symbols are the binned data points over the X-axis with 1 standard error on the Y-axis.

Table 4. The cross-correlation matrix of the 11 key parameters. ρ_s is the Spearman's rank coefficient. d_s^1 is the logarithm of the significance level of being random distribution.

Parameters		$\Gamma_{2-10\,keV}$	$\kappa_{2-10\,keV}$ (log)	$\kappa_{5100\,Å}$ (log)	λ_{Edd} (log)	Hβ FWHM (km s^{-1}) (log)	M_{BH} ($M_\odot$) (log)	α_{ox}	L_{bol} ($\times10^{+44}$) (log)	$L_{2-10\,keV}$ ($\times10^{+44}$) (log)	α_X	α_{UV}
$\Gamma_{2-10\,keV}$	ρ_s	1	0.73	0.32	0.40	−0.72	−0.33	0.39	0.05	−0.38	0.63	−0.41
	d_s^1	−∞	−8.0	−2.0	−2.0	−8.0	−2.0	−2.0	−0.0	−2.0	−6.0	−3.0
$\kappa_{2-10\,keV}$	ρ_s	0.73	1	0.64	0.60	−0.81	−0.45	0.74	0.12	−0.49	0.89	−0.59
	d_s^1	−8.0	−∞	−6.0	−5.0	−12.0	−3.0	−9.0	−0.0	−3.0	−17.0	−5.0
κ_{5100}	ρ_s	0.32	0.64	1	0.80	−0.56	−0.60	0.32	0.20	−0.24	0.64	−0.70
	d_s^1	−2.0	−6.0	−∞	−11.0	−5.0	−5.0	−2.0	−1.0	−1.0	−6.0	−8.0
λ_{Edd}	ρ_s	0.40	0.60	0.80	1	−0.40	−0.24	0.38	0.62	0.16	0.49	−0.55
	d_s^1	−2.0	−5.0	−11.0	−∞	−2.0	−1.0	−2.0	−6.0	−1.0	−4.0	−4.0
Hβ FWHM	ρ_s	−0.72	−0.81	−0.56	−0.40	1	0.64	−0.48	0.17	0.63	−0.78	0.64
	d_s^1	−8.0	−12.0	−5.0	−2.0	−∞	−6.0	−3.0	−1.0	−6.0	−11.0	−6.0
M_{BH}	ρ_s	−0.33	−0.45	−0.60	−0.24	0.64	1	−0.03	0.55	0.78	−0.56	0.66
	d_s^1	−2.0	−3.0	−5.0	−1.0	−6.0	−∞	−0.0	−4.0	−10.0	−5.0	−7.0
α_{ox}	ρ_s	0.39	0.74	0.32	0.38	−0.48	−0.03	1	0.33	−0.17	0.65	−0.27
	d_s^1	−2.0	−9.0	−2.0	−2.0	−3.0	−0.0	−∞	−2.0	−1.0	−6.0	−1.0
L_{bol}	ρ_s	0.05	0.12	0.20	0.62	0.17	0.55	0.33	1	0.78	−0.06	0.03
	d_s^1	−0.0	−0.0	−1.0	−6.0	−1.0	−4.0	−2.0	−∞	−10.0	−0.0	−0.0
$L_{2-10\,keV}$	ρ_s	−0.38	−0.49	−0.24	0.16	0.63	0.78	−0.17	0.78	1	−0.60	0.38
	d_s^1	−2.0	−3.0	−1.0	−1.0	−6.0	−10.0	−1.0	−10.0	−∞	−5.0	−2.0
α_X	ρ_s	0.63	0.89	0.64	0.49	−0.78	−0.56	0.65	−0.06	−0.60	1	−0.65
	d_s^1	−6.0	−17.0	−6.0	−4.0	−11.0	−5.0	−6.0	−0.0	−5.0	−∞	−7.0
α_{UV}	ρ_s	−0.41	−0.59	−0.70	−0.55	0.64	0.66	−0.27	0.03	0.38	−0.65	1
	d_s^1	−3.0	−5.0	−8.0	−4.0	−6.0	−7.0	−1.0	−0.0	−2.0	−7.0	−∞

following key parameters: $\Gamma_{2-10\,keV}$, $\kappa_{2-10\,keV}$, $\kappa_{5100\,Å}$, λ_{Edd}, $FWHM_{H\beta}$, M_{BH}, α_{ox}, L_{bol}, $L_{2-10\,keV}$, α_{UV} and α_X.

First, a correlation matrix was constructed as shown in Table 4. The Spearman's rank coefficient and probability of a null hypothesis are given. The table shows that there are some subgroups of parameters which are strongly coupled with each other. For example, $\kappa_{2-10\,keV}$, $\kappa_{5100\,Å}$ and λ_{Edd} are coupled; $\Gamma_{2-10\,keV}$, Hβ FWHM, α_X and $\kappa_{2-10\,keV}$ are also coupled with each other. The strong correlation between Hβ FWHM and $\kappa_{2-10\,keV}$ can be expressed by the following equation derived from a bisector regression analysis:

$$\log(\kappa_{2-10}) = (-1.22 \pm 0.12)\log(\mathrm{FWHM}) + (5.88 \pm 0.45). \quad (17)$$

There also appear to be two subgroups, one consisting of M_{BH}, L_{bol} and $L_{2-10\,keV}$ and another consisting of M_{BH}, Hβ FWHM and

$L_{2-10\,\mathrm{keV}}$. However, correlations within these subgroups are probably a result of selection effects arising from our sample selection criteria. For example, the inclusion of extremely weak $L_{2-10\,\mathrm{keV}}$ sources may weaken or eliminate the correlations between $L_{2-10\,\mathrm{keV}}$ and other parameters.

The observed properties of AGNs should be ultimately driven by the black hole mass, mass accretion rate, black hole spin and orientation angle. We have assumed the simplest Schwarzschild black hole in our model and so its spin is not considered. Uncertainties introduced by orientation angle should also be small since our sample only contains unobscured type 1 AGNs. Therefore, the remaining intrinsic parameters are just the black hole mass and mass accretion rate (or equivalently, Eddington ratio).

We can examine the correlations further by performing a PCA on the correlation matrix formed by Pearson's correlation coefficient (Pearson 1901; Boroson & Green 1992; Francis & Wills 1999). First, we include all the 11 parameters and so the dimension of the correlation matrix is 11. Therefore the outcome of the PCA must contain 11 normalized eigenvectors [principal components (PCs)], each associated with a positive eigenvalue. Each PC is a linear combination of the 11 parameters, and is orthogonal to all the other PCs. The sum of the 11 eigenvalues equals 11. A higher eigenvalue would suggest a larger fraction of correlations contained in the direction of the corresponding eigenvector.

The EIGENQL program in IDL (Interactive Data Language) v6.2 was used to perform the PCA. We found that the first three eigenvectors contain 87 per cent of the total correlations in the matrix, i.e. 53 per cent in eigenvector 1 (PC1), 25 per cent in eigenvector 2 (PC2) and 9 per cent in eigenvector 3 (PC3). To determine the actual contributors of these eigenvectors, we cross-correlated them with the 11 key parameters. Table 5 lists the Spearman's rank coefficients. It is clear that PC1 correlates/anticorrelates very well with most key parameters, except for L_{bol}. The highest correlation strength is for $\kappa_{2-10\,\mathrm{keV}}$, α_{X} and Hβ FWHM. These in turn are probably proxies for the physical variables of M_{BH} and λ_{Edd}. PC2 is dominated by L_{bol} which confirms that L_{bol} is a relatively independent variable. We have assumed that $L_{\mathrm{bol}} = \mu \dot{M} c^2$, where μ is the standard accretion efficiency of 0.057 (see Paper I), so PC2 is in effect dominated by the mass accretion rate $\dot{M}$. The contribution from the rest eigenvectors to the set of correlation is small compared to PC1 and PC2, and are therefore not important. It was also reported by Boroson (2002) that the PC1 from the correlation matrix of optical emission-line parameters is driven predominantly by the Eddington ratio, while the PC2 from the same matrix is dominated by the luminosity. Therefore, the PC1 and PC2 from our correlation matrix of the 11 parameters have a similar basis to the two eigenvectors reported by Boroson (2002).

The inclusion of λ_{Edd}, M_{BH} and L_{bol} may bias the outcome of PCA, so we performed an independent PCA by excluding λ_{Edd}, M_{BH} and L_{bol} from the correlation matrix (Grupe 2004, 2011), and so the remaining matrix only has a dimension of eight. The resultant eigenvectors were again correlated with each of the 11 parameters. The results are listed in Table 5. The two new principal eigenvectors (PC1-excl and PC-excl in Table 5) are quite similar to PC1 and PC2 in terms of correlation outcomes with the 11 parameters. This confirms our previous PCA finding that the three physical parameters λ_{Edd}, M_{BH} and L_{bol} drive the majority of the correlations.

Table 5. The cross-correlation of the eigenvectors with the 11 key parameters. The coefficients given are from the Spearman's rank test. PC1 and PC2 are the principal components from the PCA on all the 11 parameters, while PC1-excl and PC2-excl are the principal components after excluding λ_{Edd}, M_{BH} and L_{bol} from the PCA. The row 'Property' shows the percentage of correlations contained in the direction of that eigenvector.

Property	PC1 (53 per cent)	PC2 (25 per cent)	PC1-excl (62 per cent)	PC2-excl (14 per cent)
$\Gamma_{2-10\,\mathrm{keV}}$	0.71	0.03	0.75	−0.14
$\kappa_{2-10\,\mathrm{keV}}$	0.93	0.14	0.94	0.06
$\kappa_{5100\,\text{Å}}$	0.74	0.26	0.67	0.34
λ_{Edd}	0.60	0.67	0.51	0.60
Hβ FWHM	−0.89	0.17	−0.90	0.21
M_{BH}	−0.69	0.48	−0.65	0.34
α_{ox}	0.59	0.36	0.63	0.35
L_{bol}	−0.06	0.99	−0.10	0.81
$L_{2-10\,\mathrm{keV}}$	−0.60	0.76	−0.65	0.67
α_{X}	0.92	−0.03	0.93	−0.01
α_{UV}	−0.74	−0.04	−0.70	−0.17

5 THE MEAN SEDs

5.1 Diversity of the mean SEDs

In Paper I we derived the mean SED for the 12 NLS1s in our sample, and compared this with the mean SEDs of another two groups of BLS1s. We showed that the SED shape changes dramatically as the Hβ FWHM increases. Since quasar SED are not uniform, modelling their spectra and evolution using a single template such as that of Elvis et al. (1994) will mask out a large dispersion in their intrinsic properties. In our study we aim to minimize this dispersion by grouping the SED based on each of the 11 key parameters discussed in the previous section. However, since α_{UV} and α_{X} are rough estimates of the spectral shape in optical/UV and soft X-ray regions, we excluded them from the mean SED calculation.

There are 51 AGNs in our sample. For each of the nine remaining parameters, we sorted the sources according to the parameter value, and then classified the sample into three subsets so that each subset includes 17 sources. Then the BAL quasar PG 1004+130 was excluded from its subset. The SEDs constructed using Model B in this paper were first corrected for redshift, and then divided into 450 energy bins between 1 eV and 100 keV in the logarithm. Within each subset we calculated the average luminosity in every energy bin in logarithm, together with the 1σ deviation. Then we derived the mean SED for each group together with the 1σ dispersion. The same calculation was repeated for each of the nine parameters, so that there are three mean SEDs for each parameter. No special note was made for the NLS1s because their defining parameter, Hβ FWHM, is one of the nine parameters.

Fig. 14 shows our results. Each row displays the three mean SEDs divided according to the parameter shown in the panel title. The SEDs have all been renormalized to the mean luminosity at 2500 Å of each subset. To highlight the differences among these SEDs, we mark the locations of 2500 Å and 2 keV by the vertical orange lines. The relative height of these two lines directly reflects the value of α_{ox}, and the height of the bar at 2 keV shows the dispersion in α_{ox} since the co-added SEDs are all normalized at 2500 Å. We also mark the energy peak for each mean SED by the vertical thick purple line. The mean values of other parameters are given in each plot for comparison.

We find that the mean SED changes in a similar way with all the parameters except L_{bol}. The energy at which the disc emission peaks decreases along with the ratio of luminosity in the disc compared to the Comptonized components, and the 2–10 keV spectral slope.

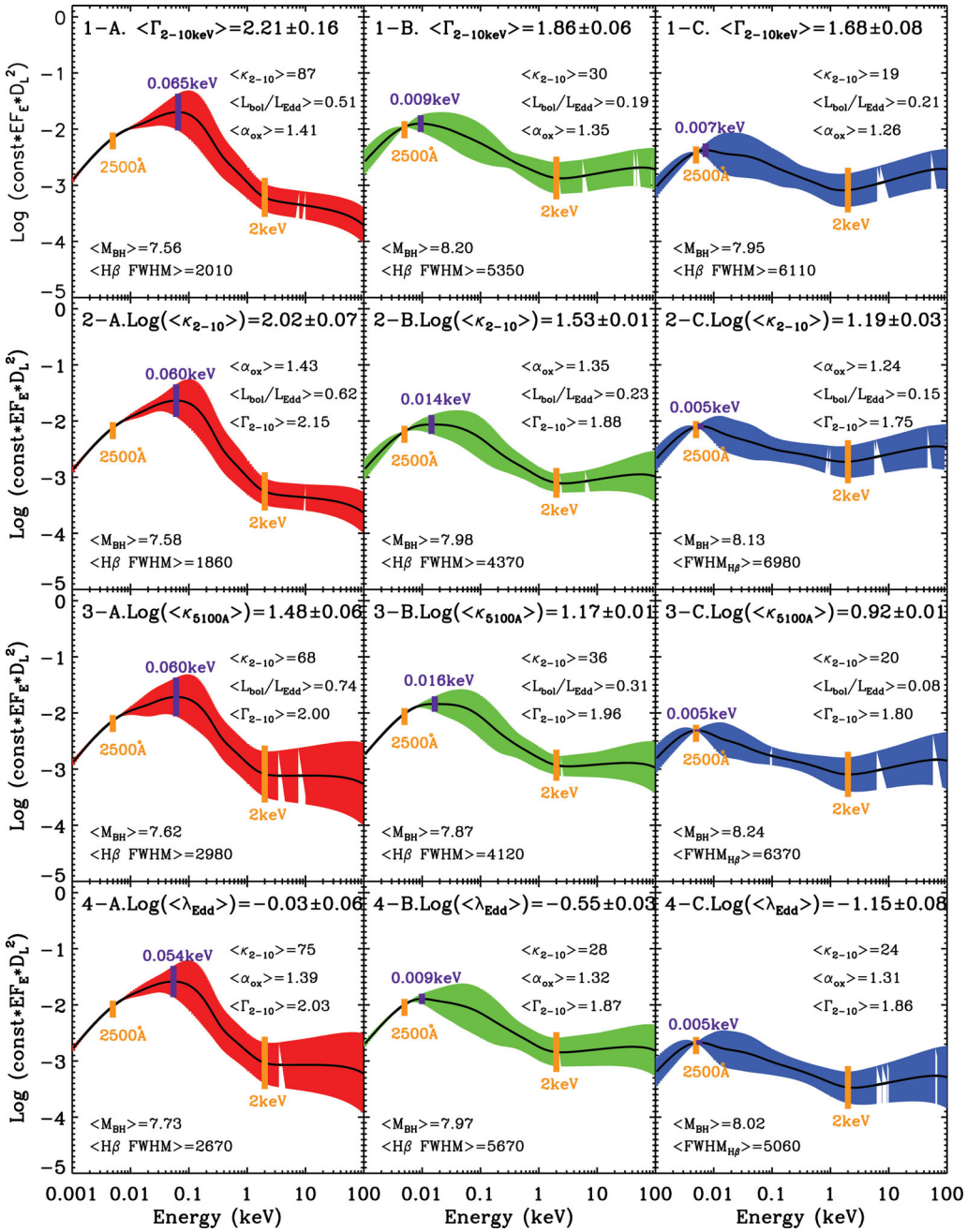

Figure 14. The AGN mean SEDs based on different values of the nine key parameters from Model B fitting (i.e. including the effect of a colour temperature correction). For each parameter, the 51 sources are sorted according to the parameter value, and then are divided into three equal subsets so that each contains 17 sources. PG 1004+130 is excluded from its subset. Finally, a mean SED is constructed for each of the three subsets after renormalizing each individual SED to the mean luminosity at 2500 Å of that subset. The three panels (A, B and C) in each row show the mean SEDs for the subsets classified by the parameter shown in the panel title. In each panel the solid curve is the mean SED, while the shaded coloured region is the $\pm 1\sigma$ deviation. The 2500-Å and 2-keV positions are marked by the vertical solid orange lines, whose relative height indicates the value of $\alpha_{\rm ox}$. The peak position of the SED is marked by the vertical solid purple line. The average values of some other parameters in that subset are also shown in the panel. Each mean SED has been rescaled by the same arbitrary constant on the Y-axis which is 1×10^{-46}. Note that the energy ranges $1.4 < E < 6$ eV and $0.3 < E < 10$ keV are covered by SDSS, OM and EPIC data, respectively, while the SED in the rest energy bands is determined from an extrapolation of the best-fitting model.

Our stringent sample selection means that these spectral differences are intrinsic rather than due to absorption/extinction.

If the SED changes are determined solely by one of the parameters considered here, then binning based on that parameter should result in the minimum dispersion within each individual binned SED and maximal difference between the three SEDs spanning the range in that parameter. However, the SED changes should ultimately be physically dependent on changes in $M_{\rm BH}$ and $\lambda_{\rm Edd}$. Since there are two dependent variables, no single parameter will completely determine the behaviour. Hence the dispersion within

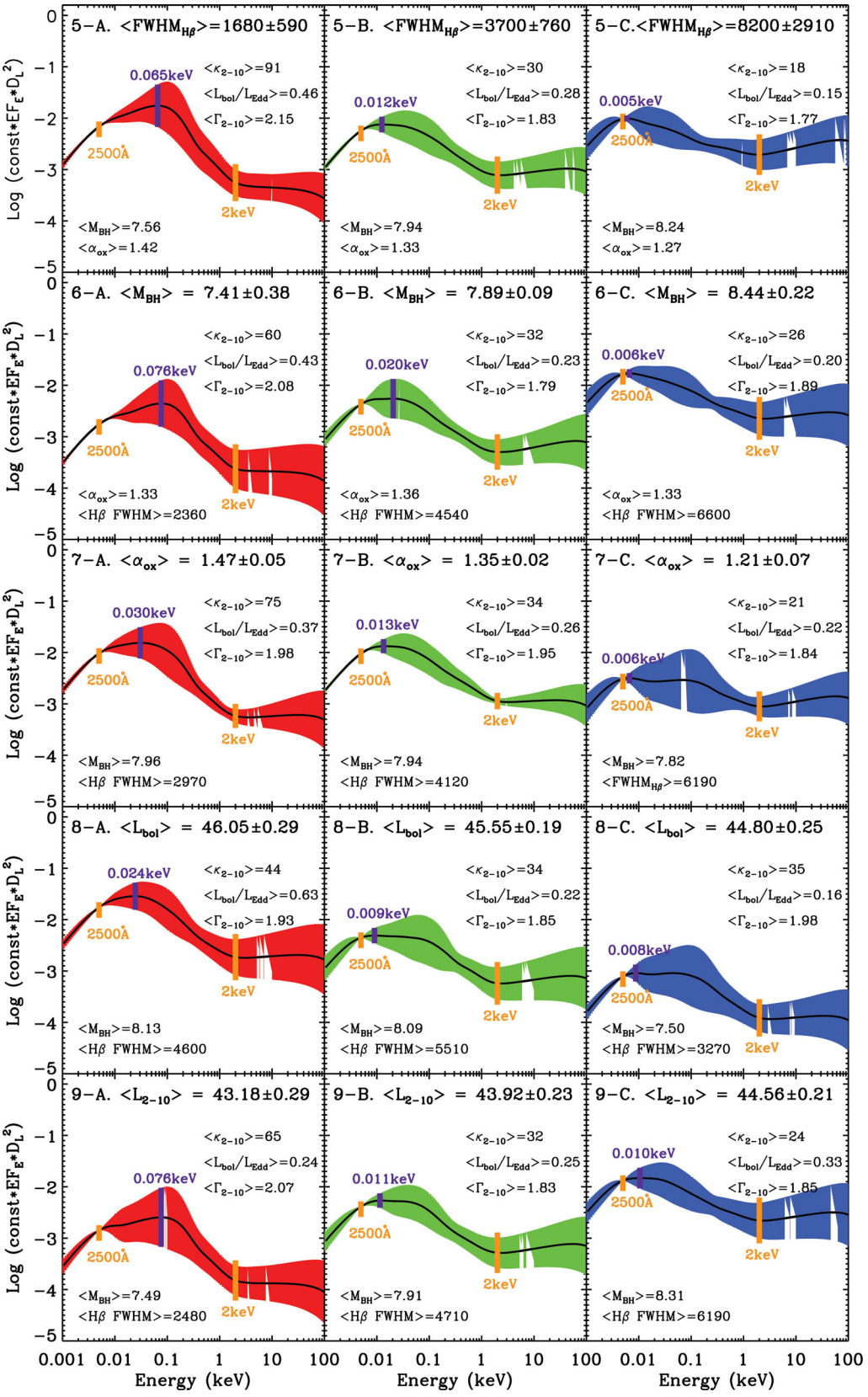

Figure 14 – *continued*

each of the three binned SEDs is minimized (and the difference between them is maximized) for composite parameters which depend on both $\lambda_{\rm Edd}$ and $M_{\rm BH}$ such as $\kappa_{2-10\,{\rm keV}}$, κ_{5100} and Hβ FWHM rather than the fundamental physical parameter $\lambda_{\rm Edd}$. Future work with larger samples can improve on this study by selecting a subsample of AGNs with different $\lambda_{\rm Edd}$ but similar $M_{\rm BH}$. Such mass selected samples would give the best comparison to the SED changes in BHBs, which all have the same mass to within a factor of $\sim$2.

5.2 Discussion of the mean SEDs

Since our SED fitting is based on a physical model, we can 'correct' for the mass dependence of the SED shape to get an estimate for the SED differences in AGNs as a function solely of $\lambda_{\rm Edd}$. This is shown in Done et al. (2012) for $M_{\rm BH} = 10^8\,{\rm M}_\odot$ and forms the basis of a direct comparison with the BHB spectral states seen for these $M_{\rm BH} = 10\,{\rm M}_\odot$ systems as $\lambda_{\rm Edd}$ changes. This has many superficial similarities to the dramatic state change seen in BHB as their luminosity increases. The SED changes from a 'low/hard state' being dominated by Comptonization, with a hard X-ray spectral index $\Gamma_{2-10\,{\rm keV}} < 2$, and the disc component peaking at rather low temperature, to a 'high/soft state' where the disc dominates the luminosity and the X-ray spectral index is softer, $\Gamma_{2-10\,{\rm keV}} \sim$ 2–2.2 (see e.g. the review by Done, Gierliński & Kubota 2007). However, this occurs at $\lambda_{\rm Edd} \sim 0.02$ for moderate changes in mass accretion rate (Maccarone 2003), an order of magnitude lower than the spectral differences seen here in the AGNs (see also the discussion in Done et al. 2012). This could indicate some subtle differences in the transition due to the very different masses, but in BHB this transition is also associated with the radio jet switching off (Fender, Belloni & Gallo 2004). If the Compton-dominated states in AGNs correspond to the low/hard state in BHB, then we would expect them to be RL. However, AGNs are RQ by a factor of 10.

This makes unlikely an identification of the two lower $\lambda_{\rm Edd}$ AGN templates as analogues to the low/hard (or intermediate state) seen in BHB. Instead, there is another state in BHB called the 'very high' or 'steep power-law state', where the disc also peaks at a lower temperature than expected, and where the Comptonized component contains a large fraction of the total luminosity (see e.g. the review by Done et al. 2007). However, this state has $\Gamma_{2-10\,{\rm keV}} > 2.5$, i.e. the hard X-ray spectra are steep. Yet these AGNs have $\Gamma_{2-10\,{\rm keV}} < 2$, as well as a soft X-ray excess component. Therefore, to match the AGN with the very high state would require that reflection and/or complex absorption modify the spectrum, producing an apparent soft X-ray excess and a hard power law from an intrinsically steep spectrum. However, the time variability properties of individual objects make it clear that these high-mass, relatively low Eddington ratio objects do indeed have two separate components: the intrinsically hard power law which is more variable on short time-scales and a soft X-ray excess which is relatively constant on these timescales but more variable over longer times (e.g. Mrk 509: Mehdipour et al. 2011; Noda et al. 2011).

Therefore, the two lowest $\lambda_{\rm Edd}$ spectra shown in Fig. 14 do not look similar to *any* state observed in BHB. Yet these sources span the typical QSO accretion rates (e.g. Steinhardt & Elvis 2010), and indeed our templates are very similar to the mean SED in Elvis et al. (1994). It seems that these most common QSO SEDs are not simply analogous to BHB accretion flows. Only the very rare AGN SEDs with the highest $\lambda_{\rm Edd}$ can be well matched to the BHB, as they are similar to the high/soft state (see also Done et al. 2012).

6 DISCUSSION

6.1 Selection effects

Biases and systematics inherent in this sample have already been discussed at length in Paper I and Paper II. The principal imposed selection effect is that sources in our sample are bright nearby AGNs ($z < 0.4$). The luminosity of our sources is higher than the average among nearby sources, but only moderate with respect to samples containing higher redshift sources (e.g. Green09; Lusso10). Our sample contains very few sources with $L_{2-10\,{\rm keV}} < 5 \times 10^{42}\,{\rm erg\,s^{-1}}$ or $\lambda_{\rm Edd} < 0.05$. As discussed in Sections 3.2.3 and 3.6.1, those very low luminosity sources may not follow the linear regression line in the $\kappa_{2-10\,{\rm keV}}$ versus $\lambda_{\rm Edd}$ plot in Fig. 6, and these sources may populate the low $L_{2-10\,{\rm keV}}$, low $\kappa_{2-10\,{\rm keV}}$ region in Fig. 12. It is also possible that these sources may not follow other correlations reported in this paper, thereby weakening the correlations between $L_{2-10\,{\rm keV}}$ and $M_{\rm BH}$ and $L_{2-10\,{\rm keV}}$ and Hβ FWHM. Further studies of large samples are required to test such possibilities.

The weak anticorrelation found between $\lambda_{\rm Edd}$ and $M_{\rm BH}$ (Table 4) also implies some selection effect. Sources having both low black hole mass and low mass accretion rate are unlikely to be included in our sample as they would be too faint. Hence, low-mass sources in our sample will have relatively high $\lambda_{\rm Edd}$. For higher mass sources, their luminosity will peak when there is a considerable supply of gas around them to be accreted. This occurs around redshift $\sim$2, and as the available gas decreases, the mass accretion rate of high-mass AGNs in the local universe is suppressed (so-called downsizing; Fanidakis et al. 2012). Therefore, in the local universe, high-mass sources should have low $\lambda_{\rm Edd}$, resulting in the weak anticorrelation found between $M_{\rm BH}$ and $\lambda_{\rm Edd}$ (Done et al. 2012).

There are also redshift selection effects. Although comparison of parameter correlations with previous work (based on larger samples) results in a general consistency, the question remains whether there could be a redshift dependence in the correlations we find. However, there are some evidence that redshift evolution in the spectral properties of AGNs may not be strong (Fan 2006).

6.2 Limitations of the model and uncertainties

There is another underlying question on whether the correlations found might arise artificially as a result of our model assumptions. We will consider this point in two ways.

First, there are no direct constraints on the parameters in our SED model. Compared with some previous work (e.g. VF07; Grupe10; Lusso10), our spectral fitting employs the least external constraints on the values of its parameters. The only parameter that is directly constrained is $M_{\rm BH}$, whose value is restricted by the FWHM of the intermediate and broad components of the Hβ emission line. However, this range often spans more than one order of magnitude, and the best-fitting $M_{\rm BH}$ did not exceed the model limits for most sources (see table C1 of Paper I). Therefore, this constraint should not be strong enough to cause systematics.

Secondly, for previously known correlations such as $\lambda_{\rm Edd}$ versus $\kappa_{2-10\,{\rm keV}}$, $\lambda_{\rm Edd}$ versus $\Gamma_{2-10\,{\rm keV}}$ and Hβ FWHM versus $\Gamma_{2-10\,{\rm keV}}$, our results are all consistent with past studies based on a variety of

AGN samples. This suggests that the reported correlations should be intrinsic and that our results are not strongly contaminated by model assumptions. As discussed in the previous sections, the differences between our results and those previously reported are mainly due to two reasons. One is our exclusion of highly obscured sources, which reduces the non-intrinsic dispersion within these correlations. The other reason is that our parameter values are derived from a detailed spectral fitting, rather than from simply applying scaling relations which will contain high uncertainties.

However, the range of values for each of the 11 key parameters discussed previously could be dominated by model uncertainties, except for $\Gamma_{2-10\,\mathrm{keV}}$, whose measurement is relatively model-independent. For this reason, we did not adopt the uncertainties returned by XSPEC, because they must be negligible compared with the model uncertainties. Such model uncertainties are very difficult to estimate, and the values of the same parameter derived from different SED models can be quite different. As an illustration, in the following paragraphs we will compare the parameter values before and after introducing a colour temperature correction into our broad-band SED model.

6.3 The effect of the colour temperature correction

The colour temperature correction is only important for sources having both a low black hole mass and a high mass accretion rate (see Done et al. 2012, and references therein). Therefore, it only affects a small fraction of all the sources in our sample, mainly the NLS1s. The main consequences of introducing a colour temperature correction by using Model B (i.e. optxagnf in XSPEC v12) are that M_{BH} increases, L_{bol} decreases and so λ_{Edd} decreases. For example, the λ_{Edd} of PG 2233+134 decreases significantly from 14 to 2.4 after using Model B, making it much less extreme. $\kappa_{2-10\,\mathrm{keV}}$ and $\kappa_{5100\text{Å}}$ also decrease due to the decrease of L_{bol}. α_{ox} changes slightly but not significantly, because the luminosity at 2500 Å is mainly constrained by the OM data (Paper I). Fig. 15 compares the distribution of these parameters between Model A (Paper I) and Model B fitting. Table 6 lists the average values of these parameters for NLS1s, BLS1s and

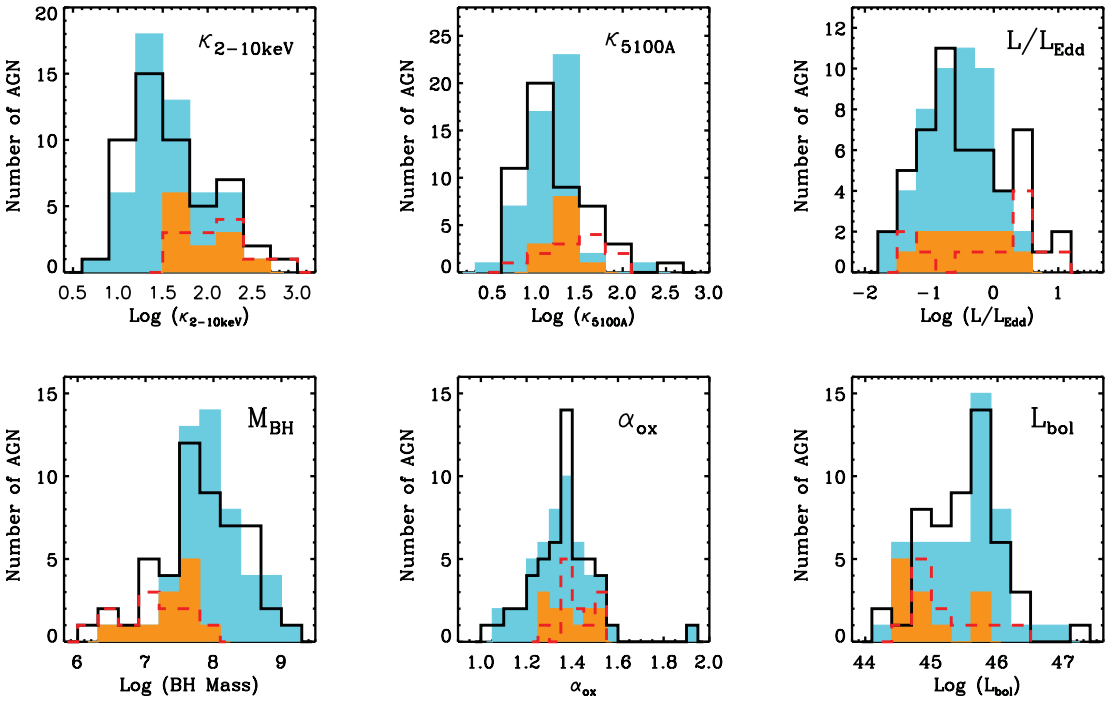

Figure 15. Comparison of parameter distributions between Model A and Model B SED fittings. In each panel the shaded cyan histogram is based on our modified SED fitting using Model B (listed in Table B2 – see Supporting Information), with the 12 NLS1s highlighted by the shaded orange region. The solid black line shows the parameter histogram for Model A fitting (listed in table 3 of Paper I), with the dashed red line indicating the 12 NLS1s.

Table 6. The average value of parameters from the best-fitting SEDs using Model A (without a colour temperature correction; Paper I) and Model B (with colour temperature correction). The values and their standard deviations are calculated separately for NLS1s, BLS1s and for the whole sample.

	NLS1s Model A	NLS1s Model B	BLS1s Model A	BLS1s Model B	Whole sample Model A	Whole sample Model B
$\langle\kappa_{2-10\,\mathrm{keV}}\rangle$	127^{+197}_{-77}	86^{+96}_{-45}	29^{+44}_{-17}	30^{+38}_{-17}	41^{+85}_{-27}	38^{+58}_{-23}
$\langle\kappa_{5100\,\text{Å}}\rangle$	29^{+37}_{-16}	20^{+13}_{-8}	13^{+17}_{-8}	14^{+14}_{-7}	16^{+23}_{-9}	15^{+14}_{-7}
$\langle\lambda_{\mathrm{Edd}}\rangle$	$0.95^{+5.33}_{-0.80}$	$0.35^{+0.99}_{-0.26}$	$0.27^{+0.81}_{-0.20}$	$0.25^{+0.52}_{-0.17}$	$0.36^{+1.42}_{-0.29}$	$0.27^{+0.61}_{-0.19}$
$\langle M_{\mathrm{BH}}\rangle$	7.11 ± 0.54	7.37 ± 0.47	8.04 ± 0.48	8.10 ± 0.41	7.83 ± 0.64	7.93 ± 0.52
$\langle\alpha_{\mathrm{ox}}\rangle$	1.42 ± 0.08	1.39 ± 0.10	1.34 ± 0.16	1.34 ± 0.15	1.36 ± 0.14	1.35 ± 0.14
$\langle L_{\mathrm{bol}}\rangle$	45.19 ± 0.54	45.02 ± 0.49	45.59 ± 0.52	45.61 ± 0.53	45.49 ± 0.55	45.47 ± 0.57

Table 7. The significance level of the difference in the NLS1–BLS1 pair (N1–B1) and population A–B pair (Pop. A–B) for values of the 11 key parameters. The two-sided KS test is applied. A smaller value suggests a greater difference within each sample division pair.

	$\Gamma_{2-10\,\mathrm{keV}}$	κ_{2-10}	$\kappa_{5100\,\text{Å}}$	λ_{Edd}	FWHM	M_{BH}	α_{ox}	L_{bol}	$L_{2-10\,\mathrm{keV}}$	α_{X}	α_{UV}
N1–B1	2×10^{-5}	5×10^{-5}	1×10^{-1}	5×10^{-1}	1×10^{-7}	1×10^{-5}	2×10^{-1}	4×10^{-3}	7×10^{-7}	1×10^{-4}	1×10^{-2}
Pop. A–B	1×10^{-4}	7×10^{-6}	5×10^{-3}	8×10^{-3}	4×10^{-11}	1×10^{-3}	1×10^{-2}	5×10^{-1}	1×10^{-2}	3×10^{-5}	3×10^{-3}

the whole sample, for both Model A and Model B fitting. This confirms that the large differences in results from the Model A and Model B fittings are mostly restricted to the NLS1s, whose colour temperature corrections are significant.

In order to further investigate the differences between using Model A and Model B, we redo all of the above cross-correlation analysis by adopting Model A parameter values from Paper I, and then we compare the statistical results in the appendices. Appendix C (see Supporting Information with the online version of the paper) shows all of the correlation plots that could in principle be modified by the differences between the Model A and Model B fittings. In each plot the dashed grey lines are for Model B fitting (this paper), compared with the solid orange lines for Model A fitting. It is clear that there are no significant changes in any of these correlation plots. This is further confirmed by the correlation matrix for Model A fitting in Appendix D (see Supporting Information with the online version of the paper). Performing a PCA on this matrix, very similar eigenvectors and eigenvalues are obtained. Appendix E (see Supporting Information) shows the mean SEDs based on the parameter values obtained from Model A fitting, which does not include the colour temperature correction. Therefore, we conclude that use of the refined Model B compared with the original Model A does not alter the main results reported in this paper, although for individual sources such as the NLS1s the refined model should be more realistic.

6.4 The correction for radiation pressure

Marconi et al. (2008) suggested that the virial mass estimates should be corrected for the effects of RP, especially for those sources with high Eddington ratios, such as the NLS1s. In our study, M_{BH} was not derived directly from the virial mass, but was only constrained by the virial masses calculated from the FWHM of the intermediate and broad components of the Hβ line. The final estimate of M_{BH} is derived from the best-fitting SED, and so there is no need to correct for the RP effect. However, we may still choose to derive the virial mass from using the FWHM of Hβ profile (narrow component subtracted), and then correct these values for the RP effect. Paper I had listed and compared these masses (M_{RP}) with the best-fitting masses (M_{BF}) from the SED fitting using Model A. The distributions of these two estimates of masses are very similar, except that the average M_{RP} is 0.4 dex higher compared with M_{BF}.

As discussed in the previous section, the SED fittings including the colour temperature correction (Model B) increases the average M_{BF} by 0.27 dex for NLS1s and by 0.05 dex for BLS1s (Table 6). Therefore, for the NLS1s using Model B fitting, the average M_{BF} is just 0.05 dex smaller than the average M_{RP}, while for the BLS1s the difference is still 0.34 dex. Furthermore, no significant difference is found in Table 4 if we substitute M_{RP} for M_{BF}, and cross-correlate with the other 10 SED parameters. The coefficients in equations (15) and (16) only differ by less than 1σ when using M_{RP} instead of M_{BF}. This suggests that the difference between M_{RP} and M_{BF} is far less than the intrinsic dispersion in any of the correlations, and so is not important in our correlation studies.

6.5 The 4000 km s^{-1} Hβ FWHM break

The FWHM$_{\mathrm{H}\beta} = 2000\,\mathrm{km\,s^{-1}}$ is the conventional but arbitrary value to distinguish between NLS1s and BLS1s (Goodrich 1989). Recently, the limit of $4000\,\mathrm{km\,s^{-1}}$ for the FWHM$_{\mathrm{H}\beta}$ was claimed to be of special interest. For example, when AGNs are divided into two populations based on FWHM$_{\mathrm{H}\beta} = 4000\,\mathrm{km\,s^{-1}}$ (population A: FWHM$_{\mathrm{H}\beta} \lesssim 4000\,\mathrm{km\,s^{-1}}$ and population B: FWHM$_{\mathrm{H}\beta} \gtrsim 4000\,\mathrm{km\,s^{-1}}$), it appeared that most RL sources are contained in population B (Sulentic et al. 2008). Compared with the RL–RQ and the NLS1–BLS1 divisions, this dividing line in FWHM also seems to be more effective in distinguishing the different SEDs (Sulentic et al. 2008). Furthermore, Zhou10a reported that in the FWHM$_{\mathrm{H}\beta}$ versus $\Gamma_{2-10\,\mathrm{keV}}$ correlation plot, there is a change in the slope at $\sim 4000\,\mathrm{km\,s^{-1}}$, consistent with our results. They also showed that the broadest iron Kα lines (those with intrinsic width $\sigma > 0.5$ keV) are all found in AGNs with FWHM$_{\mathrm{H}\beta} < 4000\,\mathrm{km\,s^{-1}}$.

In Section 3.5, we confirmed a slope change at FWHM$_{\mathrm{H}\beta} \simeq 4000\,\mathrm{km\,s^{-1}}$ in the FWHM$_{\mathrm{H}\beta}$ versus $\Gamma_{2-10\,\mathrm{keV}}$ correlation plot. All the three RL sources in our sample (purple symbols in Fig. 9) have FWHM$_{\mathrm{H}\beta} > 4000\,\mathrm{km\,s^{-1}}$. To highlight the 27 population A sources in our sample, we use the square symbol to identify these sources in all correlation plots, and we show their distribution in the histograms as the green region. The 12 NLS1s among them are shown as the red region. The two-sided Kolmogorov–Smirnov (KS) test was used to determine the significance of the difference between the distributions of the subsamples for the NLS1–BLS1 division and the population A–B division. Among the 11 key parameters, the population A–B division provides a somewhat better division for the seven parameters, $\kappa_{2-10\,\mathrm{keV}}$, $\kappa_{5100\,\text{Å}}$, λ_{Edd}, Hβ FWHM, α_{ox}, α_{X} and α_{UV}, while the NLS1–BLS1 division is better for the other parameters (see Table 7). Therefore, the population A–B division for our RQ type 1 AGN sample does not seem to be significantly better than the NLS1–BLS1 division.

7 SUMMARY AND FUTURE WORK

7.1 Summary of principal results

In this third paper in the series, we have studied the SED properties of our type 1 AGN sample. We employ a new broad-band SED model (optxagnf in XSPEC v12), which includes a colour temperature correction, to construct the SED for each source in the sample. Various parameters were obtained from the results of the SED fitting. A detailed statistical analysis was performed, which can be divided into three major parts.

(i) In the first part we studied the diverse correlations found among the SED parameters. We divided these parameters into five groups, according to previously reported correlations. Within each group we conducted a detailed cross-correlation analysis and applied several regression methods. Our results are generally in good agreement with previous work. However, as a consequence of the unobscured nature of the sample and the more reliable parameter

values that resulted from our refined spectral fitting, we were able to reduce the non-intrinsic dispersion and so obtain the intrinsic and better constrained correlations.

For example, we confirmed the linear correlation in $\log(L_{2500})$ versus $\log(L_{2\,\mathrm{keV}})$ with slope $\sim$1. The correlation of $\log(\kappa_{2-10\,\mathrm{keV}})$ with α_{ox} can be approximated using a second-order polynomial. The correlation between α_{ox} and $\log(\lambda_{\mathrm{Edd}})$ is weak and dominated by dispersion in intrinsic source properties. Some strong correlations have been confirmed, e.g. $\log(\kappa_{2-10\,\mathrm{keV}})$ versus $\log(\lambda_{\mathrm{Edd}})$, $\log(\kappa_{5100})$ versus $\log(\lambda_{\mathrm{Edd}})$, $\log(\kappa_{5100})$ versus $\log(\kappa_{2-10\,\mathrm{keV}})$, $\Gamma_{2-10\,\mathrm{keV}}$ versus $\log(\lambda_{\mathrm{Edd}})$, $\Gamma_{2-10\,\mathrm{keV}}$ versus $\log(\kappa_{5100})$, $\log(M_{\mathrm{BH}})$ versus $\log(\mathrm{FWHM}_{\mathrm{H}\beta})$ and $\log(\kappa_{2-10\,\mathrm{keV}})$ versus $\log(M_{\mathrm{BH}})$. The correlations in both $\Gamma_{2-10\,\mathrm{keV}}$ versus $\log(\mathrm{FWHM}_{\mathrm{H}\beta})$ and $\Gamma_{2-10\,\mathrm{keV}}$ versus $\log(M_{\mathrm{BH}})$ change slopes as $\Gamma_{2-10\,\mathrm{keV}}$ decreases to $\sim$1.8. The break region is $\mathrm{FWHM}_{\mathrm{H}\beta} \simeq 4000\,\mathrm{km\,s^{-1}}$ and $\log(M_{\mathrm{BH}}) \simeq 8.0$. $\Gamma_{2-10\,\mathrm{keV}}$ is almost independent of the $\mathrm{FWHM}_{\mathrm{H}\beta}$ after the break region, with a mean value of 1.8. By presenting the correlations between α_{X}, α_{UV}, α_{ox} and $L_{2-10\,\mathrm{keV}}$, we also confirmed that AGNs with bluer optical/UV spectra tend to have steeper X-ray spectra and their hard X-ray emission is also weaker. Other strong (anti)correlations were found for α_{X} and α_{UV}, such as α_{X} (α_{UV}) versus $\kappa_{2-10\,\mathrm{keV}}$, α_{X} (α_{UV}) versus $\kappa_{5100\,\text{Å}}$, α_{X} (α_{UV}) versus $\mathrm{FWHM}_{\mathrm{H}\beta}$ and α_{X} (α_{UV}) versus M_{BH}.

(ii) In the second part of our work, we performed a systematic cross-correlation study by producing the correlation matrix of the 11 key parameters: $\Gamma_{2-10\,\mathrm{keV}}$, $\kappa_{2-10\,\mathrm{keV}}$, $\kappa_{5100\,\text{Å}}$, λ_{Edd}, $\mathrm{FWHM}_{\mathrm{H}\beta}$, M_{BH}, α_{ox}, L_{bol}, $L_{2-10\,\mathrm{keV}}$, α_{X} and α_{UV}. The PCA was performed on the correlation matrix to discover the principal eigenvectors that drive most of the correlations. We found that the first two eigenvectors (PC1 and PC2) contain $\sim$80 per cent of all correlations in the matrix. PC1 strongly correlates with M_{BH}, while PC2 is dominated by L_{bol}. In addition, both PC1 and PC2 well correlate with λ_{Edd}. Thus the two principle eigenvectors are driven by M_{BH}, λ_{Edd} and L_{bol} (or equivalently $\dot{M}$). Our eigenvectors also have similar properties to the two principal eigenvectors derived by Boroson (2002) based on their optical emission-line study.

(iii) In the third part we produced various mean SEDs classified by each of the key parameters. The SED shapes are found to exhibit similar changes with most parameters except L_{bol}. This explains the strong correlations found among these key parameters. A more detailed mean SED comparison suggests that the dispersion within each of the three binned SEDs is minimized (and the difference between them is maximized) for composite parameters which depend on both λ_{Edd} and M_{BH}, such as $\kappa_{2-10\,\mathrm{keV}}$, κ_{5100} and Hβ FWHM. This is because the SED change is not determined solely by any of these key parameters. It should ultimately depend on both λ_{Edd} and M_{BH}.

(iv) To test the robustness of the main results from our correlation study, we looked at the black hole masses corrected for the effect of RP. We found no significant differences from using our best-fitting black hole masses. We also compared the correlation results between Model A (without a colour temperature correction) and Model B (including a colour temperature correction) fitting, and found that they were all very similar.

(v) The population A–B division for AGNs was compared with the NLS1–BLS1 division, but it did not prove to be a better AGN classification method.

7.2 Future work

Our sample is limited to relatively high λ_{Edd}, with few objects below $\lambda_{\mathrm{Edd}} = 0.05$. These (predominantly low-ionization nuclear emission-line region) objects are the ones expected to be the counterparts of the low/hard state in BHB. Another important extension would be to increase the sample size and include rare higher mass objects with high Eddington ratios. This would allow the SEDs to be co-added for different λ_{Edd} at a given (fixed) black hole mass, thus providing a direct comparison with the BHB states.

The major result of this study is that the SEDs of AGNs exhibit a very wide range, most plausibly as a function of mass accretion rate for a given mass black hole. This clearly shows that the so-called unified schemes, where AGNs have intrinsically identical spectra which are modified by orientation-dependent obscuration, are an oversimplification of the actual situation. In fact, unobscured AGNs can have quite different SED shapes depending on λ_{Edd} and M_{BH}.

Although not widely appreciated, this is broadly expected by the analogy of AGNs with BHB. The stellar mass black holes clearly show a dramatic change in spectral shape with λ_{Edd}, but unlike AGNs, these changes can be tracked in a single object because of the much shorter time-scale for variability. However, while the highest λ_{Edd} spectra appear similar to the disc-dominated 'high/soft state' seen in BHB, the more typical AGNs [with an SED similar to the standard quasar SED template in Elvis et al. (1994)] do not appear to have SED properties which match with any spectral state known in BBB.

This might indicate a physical break in the properties of the accretion flow between stellar mass and SMBHs. The most obvious change in physical conditions between these two mass regimes is that AGN discs are strong in the UV, and so are capable of powering substantial mass loss via a UV line-driven wind. A consequence of mass loss in the wind is that the accretion rate is no longer constant as a function of radius, causing an intrinsic change in the structure of the accretion flow (e.g. Proga, Stone & Kallman 2000). Emission/absorption/scattering processes in the wind can also change the observed properties of the spectrum (Sim et al. 2010). Further work on theoretical disc models including these effects will show whether standard AGN accretion flows are indeed sculpted by a wind.

ACKNOWLEDGMENTS

We are very grateful to Dirk Grupe for his useful comments and suggestions. CJ acknowledges financial support through Durham Doctoral Fellowship. This work is partially based on data from SDSS, whose funding is provided by the Alfred P. Sloan Foundation, the Participating Institutions, the National Science Foundation, the US Department of Energy, the National Aeronautics and Space Administration, the Japanese Monbukagakusho, the Max Planck Society and the Higher Education Funding Council for England. This work is also partially based on observations obtained with *XMM–Newton*, an ESA science mission with instruments and contributions directly funded by ESA Member States and the USA (NASA).

REFERENCES

Atlee D. W., Mathur S., 2009, ApJ, 703, 1597
Avni Y., Tananbaum H., 1982, ApJ, 262, L17
Bessell M. S., 1991, A&A, 242, L17
Bian W.-H., 2005, Chinese J. Astron. Astrophys., 5, 289
Boller T., Brandt W. N., Fink H., 1996, A&A, 305, 53
Boroson T. A., 2002, ApJ, 565, 78
Boroson T. A., Green R. F., 1992, ApJS, 80, 109
Brandt W. N., Mathur S., Elvis M., 1997, MNRAS, 285, L25

Brocksopp C., Starling R. L. C., Schady P., Mason K. O., Romero-Colmenero E., Puchnarewicz E. M., 2006, MNRAS, 366, 953
Davis S. W., Hubeny I., 2006, ApJS, 164, 530
Davis S. W., Done C., Blaes O. M., 2006, ApJ, 647, 525
Done C., Gierliński M., 2005, MNRAS, 364, 208
Done C., Gierliński M., Kubota A., 2007, A&AR, 15, 1
Done C., Davis S., Jin C., Blaes O., Ward M., 2012, MNRAS, 420, 1848
Elvis M. et al., 1994, ApJS, 95, 1
Fan X., 2006, New Astron. Rev., 50, 665
Fanidakis N. et al., 2012, MNRAS, 419, 2797
Fender R. P., Belloni T. M., Gallo E., 2004, MNRAS, 355, 1105
Francis P. J., Wills B. J., 1999, in Ferland G., Baldwin J., eds, ASP Conf. Ser. Vol. 162, Quasars and Cosmology. Astron. Soc. Pac., San Francisco, p. 363
Francis P. J., Hewett P. C., Foltz C. B., Chaffee F. H., Weymann R. J., Morris S. L., 1991, ApJ, 373, 465
George I. M., Turner T. J., Yaqoob T., Netzer H., Laor A., Mushotzky R. F., Nandra K., Takahashi T., 2000, ApJ, 531, 52
Gierliński M., Middleton M., Ward M., Done C., 2008, Nat, 455, 369
Goodrich R. W., 1989, ApJ, 342, 224
Green P. J. et al., 1995, ApJ, 450, 51
Green P. J. et al., 2009, ApJ, 690, 644 (Green09)
Grupe D., 2004, AJ, 127, 1799
Grupe D., 2011, in Colpi M., Gallo L., Grupe D., Komossa S., Leighly K., Mathur S., eds, Proc. Sci. Vol. NLS1, Narrow-Line Seyfert 1 Galaxies and Their Place in the Universe. Pos, Trieste
Grupe D., Beuermann K., Thomas H.-C., Mannheim K., Fink H. H., 1998, A&A, 330, 25
Grupe D., Beuermann K., Mannheim K., Thomas H.-C., 1999, A&A, 350, 805
Grupe D., Komossa S., Leighly K. M., Page K. L., 2010, ApJS, 187, 64 (Grupe10)
Hasinger G., 2005, in Merloni A., Nayakshin S., Sunyaev R. A., eds, Growing Black Holes: Accretion in a Cosmological Context. Springer-Verlag, Berlin, p. 418 (Hasinger05)
Hopkins P. F., Richards G. T., Hernquist L., 2007, ApJ, 654, 731 (Hopkins07)
Isobe T., Feigelson E. D., Akritas M. G., Babu G. J., 1990, ApJ, 364, 104
Jin C., Done C., Ward M., Gierliński M., Mullaney J., 2009, MNRAS, 398, L16
Jin C., Ward M., Done C., Gelbord J. M., 2012a, MNRAS, 420, 1825 (Paper I)
Jin C., Ward M., Done C., 2012b, MNRAS, 422, 3268 (Paper II)
Just D. W., Brandt W. N., Shemmer O., Steffen A. T., Schneider D. P., Chartas G., Garmire G. P., 2007, ApJ, 665, 1004
Kaspi S., Smith P. S., Netzer H., Maoz D., Jannuzi B., Giveon U., 2000, ApJ, 533, 631
Kelly B. C., Bechtold J., Trump J. R., Vestergaard M., Siemiginowska A., 2008, ApJS, 176, 355
Kollatschny W., 2003, A&A, 407, 461
Kollatschny W., Bischoff K., Robinson E. L., Welsh W. F., Hill G. J., 2001, A&A, 379, 125
La Franca F., Franceschini A., Cristiani S., Vio R., 1995, A&A, 299, 19
Landt H., Elvis M., Ward M. J., Bentz M. C., Korista K. T., Karovska M., 2011, MNRAS, 414, 218
Laor A., Fiore F., Elvis M., Wilkes B. J., McDowell J. C., 1994, ApJ, 435, 611
Laor A., Fiore F., Elvis M., Wilkes B. J., McDowell J. C., 1997, ApJ, 477, 93
Leighly K. M., 1999, ApJS, 125, 317
Lu Y., Yu Q., 1999, ApJ, 526, L5
Lusso E. et al., 2010, A&A, 512, 34 (Lusso10)
Maccarone T. J., 2003, A&A, 409, 697
McHardy I. M., Koerding E., Knigge C., Uttley P., Fender R. P., 2006, Nat, 444, 730
Marconi A., Risaliti G., Gilli R., Hunt L. K., Maiolino R., Salvati M., 2004, MNRAS, 351, 169 (Marconi04)
Marconi A., Axon D. J., Maiolino R., Nagao T., Pastorini G., Pietrini P., Robinson A., Torricelli G., 2008, ApJ, 678, 693
Mehdipour M. et al., 2011, A&A, 534, 39
Meyer-Hofmeister E., Liu B. F., Meyer F., 2009, A&A, 508, 329
Middleton M., Done C., Gierliński M., 2007, MNRAS, 381, 1426
Middleton M., Done C., Ward M., Gierliński M., Schurch N., 2009, MNRAS, 394, 250
Miller B. P., Brandt W. N., Gallagher S. C., Laor A., Wills B. J., Garmire G. P., Schneider D. P., 2006, ApJ, 652, 163
Noda H., Makishima K., Yamada S., Torii S., Sakurai S., Nakazawa K., 2011, PASJ, 63, 925
Pearson K., 1901, Philos. Magazine, 2, 559
Peterson B. M. et al., 2004, ApJ, 613, 682
Piconcelli E., Jimenez-Bailón E., Guainazzi M., Schartel N., Rodríguez-Pascual P. M., Santos-Lleó M., 2005, A&A, 432, 15
Porquet D., Reeves J. N., O'Brien P., Brinkmann W., 2004, A&A, 422, 85
Proga D., Stone J. M., Kallman T. R., 2000, ApJ, 543, 686
Puchnarewicz E. M. et al., 1992, MNRAS, 256, 589
Reeves J. N., Turner M. J. L., 2000, MNRAS, 316, 234
Remillard R. A., McClintock J. E., 2006, ARA&A, 44, 49
Richards G. T. et al., 2006, ApJS, 166, 470
Ross R. R., Fabian A. C., Mineshige S., 1992, MNRAS, 258, 189
Sanders D. B., Phinney E. S., Neugebauer G., Soifer B. T., Matthews K., 1989, ApJ, 347, 29
Shang Z. et al., 2005, ApJ, 619, 41
Shemmer O., Brandt W. N., Netzer H., Maiolino R., Kaspi S., 2006, ApJ, 646, L29 (S06)
Shemmer O., Brandt W. N., Netzer H., Maiolino R., Kaspi S., 2008, ApJ, 682, 81 (S08)
Sim S. A., Miller L., Long K. S., Turner T. J., Reeves J. N., 2010, MNRAS, 404, 1369
Steffen A. T., Strateva I., Brandt W. N., Alexander D. M., Koekemoer A. M., Lehmer B. D., Schneider D. P., Vignali C., 2006, AJ, 131, 2826
Steinhardt C. L., Elvis M., 2010, MNRAS, 402, 2637
Strateva I. V., Brandt W. N., Schneider D. P., Vanden B., Daniel G., Vignali C., 2005, AJ, 130, 387
Sulentic J. W., Zamfir S., Marziani P., Dultzin D., 2008, Rev. Mex. Astron. Astrofis. Conf. Ser., 32, 51
Tananbaum H. et al., 1979, ApJ, 234, L9
Tang S., Zhang S., Hopkins P. F., 2007, MNRAS, 377, 1113 (Tang07)
Trump J. R. et al., 2011, ApJ, 733, 60
Vanden Berk D. E. et al., 2001, AJ, 122, 549
Vasudevan R. V., Fabian A. C., 2007, MNRAS, 381, 1235 (VF07)
Vasudevan R. V., Fabian A. C., 2009, MNRAS, 392, 1124 (VF09)
Vignali C., Brandt W. N., Schneider D. P., 2003, AJ, 125, 433
Walter R., Fink H. H., 1993, A&A, 274, 105
Wandel A., Peterson B. M., Malkan M. A., 1999, ApJ, 526, 579
Wang J.-M., Watarai K., Mineshige S., 2004, ApJ, 607, L107
Wilkes B. J., Elvis M., 1987, 323, 243
Wilkes B. J., Tananbaum H., Worrall D. M., Avni Y., Oey M. S., Flanagan J., 1994, ApJS, 92, 53
Woo J., Urry C. M., 2002, ApJ, 579, 530
Young M., Elvis M., Risaliti G., 2009, ApJS, 183, 17
Yuan W., Siebert J., Brinkmann W., 1998, A&A, 334, 498 (Yuan98)
Zheng W., Kriss G. A., Telfer R. C., Grimes J. P., Davidsen A. F., 1997, ApJ, 475, 469
Zhou X., Zhang S., 2010a, ApJ, 713, L11 (Zhou10a)
Zhou X., Zhao Y., 2010b, ApJ, 720, L206 (Zhou10b)
Zhou H., Wang T., Yuan W., Lu H., Dong X., Wang J., Lu Y., 2006, ApJS, 166, 128

SUPPORTING INFORMATION

Additional Supporting Information may be found in the online version of this article.

Table A1. A summary of references about the correlations among the most important AGN SED parameters.
Table B1. Broad-band SED fitting parameters.

Table B2. Key parameters from Model B fitting.
Figures C1–C10. Parameter cross-correlations using values from Model A fitting.
Table D1. The cross-correlation matrix of the nine key parameters based on Model A data from Jin et al. (2011).
Figure E1. The AGN mean SEDs based on different values of the nine key parameters from Model A fitting in Paper I.

This paper has been typeset from a TEX/LATEX file prepared by the author.